An- Najah National University

Faculty of Graduate Studies

Carbon Nanofibers: Graphene Nanoplateletes Composite as Supercapacitor Electrode Using KOH Aqueous Electrolyte

By

Sabreen Jarrar

Supervisor

Dr. Allan Daraghmeh

Co- Supervisor

Dr. Iyad Saadeddin

This Thesis is Submitted in Partial Fulfillment of Requirements for the Degree of Master of Physics, Faculty of Graduate Studies, An- Najah National University, Nablus - Palestine.

2020

Carbon Nanofibers/ Graphene Nanoplateletes Composite as Supercapacitor Electrode Using KOH Aqueous Electrolyte

By

Sabreen Jarrar

This Thesis was Defensed Successfully on 28/9/2020 and approved by:

Defense Committee Members	**Signature**
1. Dr. Allan Daraghmeh / Supervisor	.....
2. Dr. Iyad Saadeddin / Co- Supervisor	.....
3. Dr. Hussein Shanak / External Examiner	.....
4. Prof. Sami Al- Jaber / Internal Examiner	.....

Acknowledgment

I would like to pay my special regards to president of An- Najah University Prof. Dr. Maher Al- Natsheh for supporting and encouraging this experimental work. I wish to express my sincere appreciation to my supervisors, Dr. Allan Daraghmeh and Dr. Iyad Saadeddin, who guided and encouraged me to be professional in this work and do the right thing even when the work became hard and tough. Without their persistent help, the aim of this thesis would not have been realized. I would like to thank Prof. Dr. Sami Al- Jaber for his directions, advices and supporting.

Also, I would like to acknowledge Dr. Llorenc Servera in Barcelona University and Dr. Shahazad Awan in University of Ulster for providing assistance to get a completed professional work. In addition, I would like to acknowledge Department of Chemistry, in particular Nafeth Dweakat and Department of Physics at An- Najah University for offering help to finish this work as soon as possible.

Finally, I wish to acknowledge the support and great love of my family, who support me to keep going on to achieve the goal of this thesis.

الإقرار

انا الموقعة ادناه، مقدمة الرسالة التي تحمل العنوان:

Carbon Nanofibers/ Graphene Nanoplateletes Composite as Supercapacitor Electrode Using KOH Aqueous Electrolyte

أقر بأن ما اشتملت عليه هذه الرسالة إنما هي نتاج جهدي الخاص، باستثناء ما تمت الإشارة إليه حيثما ورد، وأن هذه الرسالة ككل، أو أي جزء منها لم يُقدم لنيل أية درجة أو لقب علمي أو بحثي لدى أي مؤسسة تعليمية أو بحثية أخرى.

Declaration

The work provided in this thesis, unless otherwise referenced, is the researcher's own work, and has not been submitted elsewhere for any other degree or qualification.

Student's Name: **اسم الطالب:** صابرين صبري جرار

Signature: **التوقيع:** صابرين

Date: **التاريخ:** ٢٨/ ٩/ ٢٠٢٠م

Table of Contents

No.	Content	Page
	Acknowledgments	Iii
	Declaration	Iv
	List of Tables	Vii
	List of Figures	Viii
	List of Abbreviations	Xi
	Abstract	Xii
	Chapter One: Introduction	1
1.1	Review	1
1.2	Components of SCs	5
1.2.1	Electrodes	6
1.2.2	Electrolyte	8
1.2.3	Separator	9
1.3	Principle and mechanism	9
1.4	Types of SCs	12
1.4.1	Electric double layer capacitors (EDLCs)	12
1.4.2	Pseudocapacitors	13
1.4.3	Hybrid capacitors	14
1.5	Literature survey	16
1.6	Why carbon nanofibers and graphene nanoplateletes have been used as electrodes?	20
1.7	Objectives of this thesis	23
1.8	Thesis Structure	24
	Chapter Two: Theory	26
2.1	Electrochemical characterization	27
2.1.1	Cyclic voltammetry (CV)	28
2.1.2	Galvanostatic charge/discharge (GCD)	30
2.1.3	Electrodynamic impedance spectroscopy (EIS)	32
2.2	Surface, morphology and structural characterization	35
2.2.1	Brunauer- Emmett- Teller (BET), Barrett- Joyner-Halenda (BJH) methods	35
	Chapter Three: Experimental	43
3.1	Materials and setup devices	43
3.1.1	Materials	43
3.1.2	Setup devices	43
3.2	Preparation of electrodes by blade method	45
3.3	Preparation of aqueous electrolyte	46
3.4	Methodology of electrochemical calculations	47
3.5	Surface and morphology texture measurements	49
3.5.1	Surface characterization	49

3.5.1.1	BET analyzer and BJH method	49
3.5.2	Morphology characterization	50
3.5.2.1	Scanning Electron Microscope (SEM)	50
3.5.2.2	Transmission Electron Microscope (TEM)	51
	Chapter Four: Results and Discussion	53
4.1	Electrochemical behavior	53
4.1.1	Cyclic voltammetry behavior	53
4.1.2	Charge/ discharge (GCD) behavior	58
4.1.3	Electrochemical impedance behavior	67
4.2	Structural, morphological behavior and pore texture	77
4.2.1	Structural and morphological behavior	77
4.2.2	Pore texture of electrode materials	79
	Chapter Five: Conclusion	91
	References	93
	الملخص	ب

List of Tables

No.	Tittle	Page
Table 1.1	Comparison between energy sources	4
Table 3.1	Materials used in experiment	43
Table 3.2	Devices used in experiment	44
Table 4.1	C_S (F/ g) from CV for CNF/ GNP composites with different weight concentration of GNPs at different scan rates	56
Table 4.2	C_S (F/ g) from GCD for CNF/ GNP composites with different concentration of GNPs at different specific currents	62
Table 4.3	Power density and energy density for CNF/ GNP composites for different GNP weight concentration measured at different discharge current	66
Table 4.4	Resistances and C_S comparison of the samples by EIS method	69
Table 4.5	Physicochemical parameters of the samples	82
Table 4.6	Pore size for CNF/ GNP composites with different GNP concentration	88

List of Figures

No.	Tittle	Page
Figure 1.1	Ragone plot	1
Figure 1.2	Schematic of types of pore size	4
Figure 1.3	Schematic of representation of SCs	5
Figure 1.4	Schematic of mechanism of how SCs work	10
Figure 1.5	Models for potential of ions between electrodes and electrolyte (**a)** Helmholtz, **(b**) Gouy- Chapman and **(c**) Stern models	11
Figure 1.6	Schematic of types of SCs: **(a**) EDLC, **(b)** Pseudocapacitor	12
Figure 1.7	Types of pseudocapacitors	13
Figure 1.8	Schematic of hybrid supercapacitors	15
Figure 1.9	CNF structure (**a**) Schematic of the shape, (**b)** CNF structure by TEM	21
Figure 1.10	GNP structure (**a)** Schematic of the shape, (**b)** GNP structure by TEM	22
Figure 2.1	Difference in CV curve for **(a)** EDLC, **(b**) Pseudocapacitor	28
Figure 2.2	(**a**) Schematic equivalent circuit for double layer capacitor and (**b**) compact and diffuse capacitances for one electrode according to Stern model	29
Figure 2.3	Galvanostatic charge/ discharge curve for supercapacitor	30
Figure 2.4	Components of Nyquist plot for SC	34
Figure 2.5	BET plot	36
Figure 2.6	Types of adsorption isotherm	38
Figure 2.7	T- plot in the presence of (**a**) mesopores, (**b**) micropores and (**c**) external area and micropores	41
Figure 3.1	Devices used in experimental work: **(a)** press and molding machine, **(b)** balance, **(c)** magnetic stirrer, **(d)** oven, **(e**) ultrasonic, **(f)** Swagelok cell, **(g)** mortar and **(h)** potentiostate	44
Figure 3.2	Prepared electrode discs	46
Figure 3.3	Preparation 1M KOH	47
Figure 3.4	Swagelok cell assembling	48
Figure 3.5	potentiostate connection	48
Figure 3.6	BET analyzer (TriStar 3000 V6. 04A)	50
Figure 3.7	SEM (Jeol J- 7100)	51
Figure 3.8	TEM (Jeol 2011)	52

Figure 4.1	CV curves at different scan rates (5, 10, 20, 50 and 100 mV/ s) for CNF/ GNP composite with GNP weight percent of (**a)** 10%, **(b)** 30%, (**c)** 50%, (**d)** 70%, (**e**) 90% and (**f**) CV at scan rate 5 mV/ s foe all samples	55
Figure 4.2	Comparison of C_S at different scan rates for different concentration of GNPs	56
Figure 4.3	Specific capacitance and GNP concentration at different scan rates	57
Figure 4.4	Stability of CV at scan rate 100 mV/ s for 100 cycle for CNF/ GNP composites with GNP weight percent of (**a)** 10%, (**b)** 30%, **(c)** 50%, (**d)** 70% and (**e**) 90%	58
Figure 4.5	GCDs for CNF/ GNP composites at different constant specific current with GNP percentage weight of **(a)** 10%, **(b)** 30%, **(c**) 50%, **(d**) 70% and (**e**) 90%	60
Figure 4.6	GCD comparison at specific current (0.42 A/ g) of different concentration of GNPs	61
Figure 4.7	C_S for CNF/ GNP composites at different specific currents and different concentration of GNPs	62
Figure 4.8	Variation of voltage drop with discharge currents for different concentration of GNPs and shows the variation of ESR with percent content of GNP	64
Figure 4.9	Charge/ discharge cycling stability at constant specific current (1.43 A/ g) for 1500 cycle for CNF/ GNP composites with different concentration of GNPs	64
Figure 4.10	Ragone plot of power density against energy density for different concentration of GNPs at different discharging current	66
Figure 4.11	(**a**) Nyquist plot for CNF/ GNP composites with different concentration of GNPs and (**b**) Nyquist plot for GNP sample	68
Figure 4.12	Comparison for all samples by EIS (**a**) specific capacitance, and (**b)** phase angle as a function of logarithm of frequency	72
Figure 4.13	(**a)** Real and (**b)** imaginary parts against logarithm of frequency, respectively for all samples	75
Figure 4.14	SEM images for CNF/ GNP composites with different weight concentration of GNP **(a)** 10% GNP, **(b)** 30% GNP, **(c**) 50% GNP and **(d)** 70% GNP	77

Figure 4.15	TEM images for CNF/ GNP composites with different concentration of GNP **(a)** 10% GNP, (**b)** 30% GNP, **(c)** 50% GNP and (**d)** 70% GNP	78
Figure 4.16	(**a)** Nitrogen isotherms and **(b)** SSA from BET plot for CNF/ GNP composites with different weight concentration of GNPs	80
Figure 4.17	T- plot for CNF/ GNP composites with different concentration pf GNP	85
Figure 4.18	PSD by BJH desorption $\frac{dV}{dlogD}$	87

List of Abbreviations

Abbreviation	Nomenclature
SC	Supercapacitor
ESR	Equivalent series resistance
SSA	Specific surface area
PSD	Pore size distribution
C	Capacitance
C_S	Specific capacitance
P	Power density
E	Energy density
PTFE	Poly-tetrafluoroethylene
PVDC	Polyvynilidene chloride
PVDF	Polyvynilidene fluoride
LCP	Liquid crystalline polymer
PPy	Polypyrrole
AC	Active carbon
CNF	Carbon nanofiber
CNT	Carbon nanotube
GNP	Graphene nanoplatelete
ACNF	Activated carbon nanofiber
MCNT	Multiple wall carbon nanotube
IHP	Inner Helmholtz plane
OHP	Outer Helmholtz plane
EDLC	Electric double layer capacitor
CV	Cyclic voltammetry
GCD	Galvanostatic charge/ discharge
EIS	Electrochemical impedance spectroscopy
S	Scan rate
BET	Brunauer- Emmett- Teller
BJH	Barrett- Joyner- Halenda
SEM	Scanning electron microscope
TEM	Transmission electron microscope
IUPAC	International Union of Pure and Applied Chemistry
STP	Standard temperature pressure

Carbon Nanofibers/ Graphene Nanoplateletes Composite as Supercapacitor Electrode Using KOH Aqueous Electrolyte

By
Sabreen Jarrar
Supervisor
Dr. Allan Daraghmeh
Co- Supervisor
Dr. Iyad Saadeddin

Abstract

In this thesis, supercapacitor composite pallet electrodes had been prepared using different concentrations of carbon nanofibers and graphene nanoplateletes. The percentage weight of carbon nanofibers/ graphene nanoplateletes were changed from 90%/ 10% to 10%/ 90%, in steps of 20%.

Electrochemical characterization had been characterized by cyclic voltammetry, galvanostatic charge/ discharge and electrochemical impedance spectroscopy methods in 1M KOH aqueous electrolyte.

The specific capacitance was found to increase with increasing graphene nanoplateletes, which was increased from 47.0 to 119.7 F/g as graphene nanoplateletes increased from 10 to 90% weight at scan rate 5 mV/s by cyclic voltammetry method.

The power and energy densities were evaluated from galvanostatic charge/ discharge method. Power and energy densities were increased with increasing graphene nanoplateletes concentration up to 70% then decreased when weight of graphene nanoplateletes increased to 90 % weight; the power density increased from 528.33 to 1095.43 W/kg, then decreased to

956.97 W/kg. The energy density increased from 2.32 to 5.26 Wh/kg, then decreased to 5.05 Wh/kg.

Finally, equivalent series resistance was calculated from electrochemical impedance spectroscopy, which was found to increase with increasing graphene nanoplateletes concentrations up to 70%, then increases when graphene nanoplateletes increased to 90% weight. The equivalent series resistance was found to decrease from 1.48 to 0.632 Ω, then increases to 1.26 Ω as graphene nanoplateletes weight increases to 90%.

The optimized composition in terms of best specific capacitance, power density, energy density and equivalent series resistance was 30%/ 70% of carbon nanofibers/ graphene nanoplateletes, which corresponds to 102.2 F/g, 1095.43 W/kg, 5.26 Wh/kg and 0.632 Ω, respectively.

The specific surface area, pore size distribution and morphology structure of the prepared composites had been investigated by Brunauer- Emmett-Teller, Barrett- Joyner- Halenda, Harkins- Jura methods and scanning electron microscope.

It is found that the specific surface area increases with increasing graphene nanoplateletes concentrations. It was increased from 271.27 to 665.93 m^2/g as graphene nanoplateletes changed from 10% to 90% weight.

Total pore volume increases with increasing graphene nanoplateletes weight up to 70%, then it decreases as the concentration of graphene

nanoplateletes increases to 90%. The total pore volume increased from 1.22 to 1.72 cm^3/g, then it decreased to 1.33 cm^3/g.

Furthermore, micro, ultra- micro and mesopore volumes were found to increase by increasing graphene nanoplateletes concentrations from 10 to 90%. Micropore volume increases from 0.023 to 0.08 cm^3/g, ultra-micropore volume increases from 0.023 to 0.28 cm^3/g and mesopore volume increases from 0.55 to 0.88 cm^3/g when graphene nanoplateletes increase from 10% to 90% weight, respectively.

Finally, Macropore volume increases with increasing graphene nanoplateletes from 10% to 30%, which decreases from 0.64 to 0.29 cm^3/g, and then increases up to 70% weight of graphene nanoplateletes, which increases from 0.29 to 0.88 cm^3/g, then it decreases for graphene nanoplateletes 90% weight; 0.33 cm^3/g.

The best structural characterization was found for 70% weight of graphene nanoplateletes, which has the highest total pore volume (1.72 cm^3/g) and the highest macropore volume (0.88 cm^3/g). Also, it has optimized higher specific surface area, micropore, ultra- micropore and mesopore volumes which was 528.52 m^2/g, 0.0614 cm^3/g, 0.234 cm^3/g and 0.78 cm^3/g, respectively.

Chapter One
Introduction

1.1: Review

Nowadays, energy sources attract the attention of many investigators in the current researches. Fuel cells, batteries and conventional capacitors store energy which is used in devices and applications. However, substantial effort is being made towards finding and developing new storage energy devices which achieve high power density, high energy density and has long life cycle [1- 4]. Recently, supercapacitors (SCs), is considered as a new source of storing energy that fills the gap between conventional capacitors and batteries as shown in Ragone plot (figure 1.1) [5]. Ragone plot shows the relation between energy and power densities of the energy sources: Fuel cells, batteries, conventional capacitors and SCs.

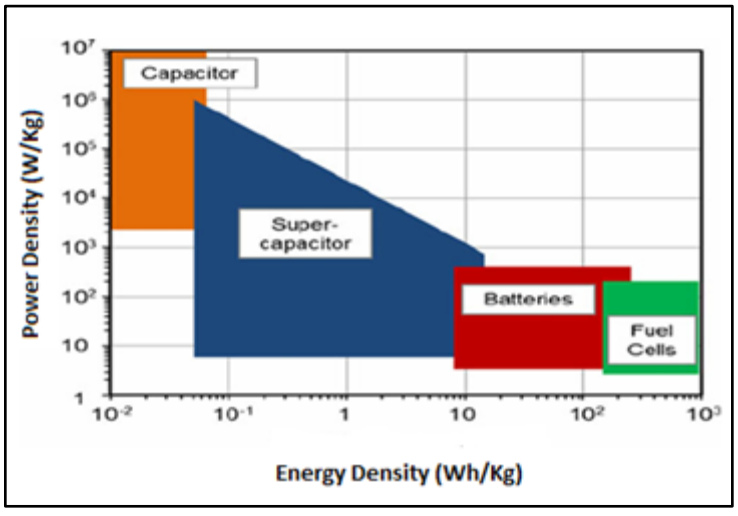

Fig. 1.1: Ragone plot

Batteries are electrochemical cells which store energy electrochemically by oxidation/reduction reaction (redox reaction). It consists of two electrodes with conductive electrolyte between them. Lithium-ion batteries are the best type of batteries which achieve high energy density (120- 170Wh/kg). The potential of the batteries during the charging process is constant so its energy density is high relative to the other energy sources ($E = Q\,V$, where Q is the charge density and V is the potential). However, its power density, charge/ discharge rate is very low due to the limited diffusion of the ions in the surface of the electrodes, and it is toxic due to chemical reaction [1, 6- 10].

Fuel cells convert the chemical energy to electrical energy. This type of energy sources consists of a cathode, an anode and electrolyte. The used electrolyte could be aqueous electrolyte, polymer membrane and ceramic oxide. Fuel cells give the highest value of energy density above 500 Wh/kg. However, its power density is very low. One of the most popular fuel cell is the hydrogen proton exchange membrane (PEM) [6].

Conventional capacitors are electrostatic capacitors that store energy in the electric field which is established between the plates of the capacitor. Two conducting electrodes which are separated by dielectric layer typical in conventional capacitors. This type of capacitors can charge/discharge very quickly so it can achieve a very high power density (5000 W/kg). But its energy density is very low which is in the range of (0.01 – 0.05 Wh/kg),

because its potential is increasing linearly during charging process. So, its energy density is half the value of batteries ($E = \frac{1}{2} Q V$) [6, 7, 9].

SCs (called also ultracapcaitors), are electrochemical storage energy devices. Which lie in the range between conventional capacitors and batteries as shown in Figure 1.1. SCs have higher energy density relative to conventional capacitors, and higher power density relative to batteries. Also, SCs can reach full charge/discharge process in seconds. And it has a very long life cycle; it can repeat charge/discharge cycles up to 1 million times [9, 11- 14]. Table 1.1 [6] shows comparison between the properties of the three energy sources.

For SC properties; it is promising to achieve high energy density while keeping the value of power density as high as possible, by enhancing the parameters affecting these properties. The performance of SC is controlled by increasing specific capacitance (C_S), voltage window (operating voltage) and decreasing equivalent series resistance (ESR) [15- 17].

C_S depends on the electrode materials which are used in SCs. Specific surface area (SSA), total pore volume (V_{tot}), wetting behavior of pores and pore size distribution (PSD) determine the dominant pores which give the highest contribution to performance of C_S [15, 17, 18].

Table (1.1): Comparison between energy sources

Parameters	Conventional capacitors	Supercapacitors	Batteries	Fuel cells
Charge/discharge time	1 ps - 1 ms	1 ms - 1 s	1 - 10 hours	Not applicable
Life cycle (cycles)	More than 1 million	Up to 1 million	150 – 2000	Not applicable
Energy density (Wh/kg)	0.01- 0.3	0.5- 20	30- 265	500- 2000
Power density (W/kg)	> 5000	5000- 10000	100- 3000	1- 1000

The International Union of Pure and Applied Chemistry (IUPAC) classify three types of pore size: macropores (50– 80 nm), mesopores (2– 50 nm) and micropores (less than 2 nm) [2, 3, 19] as shown in figure 1.2 [20].

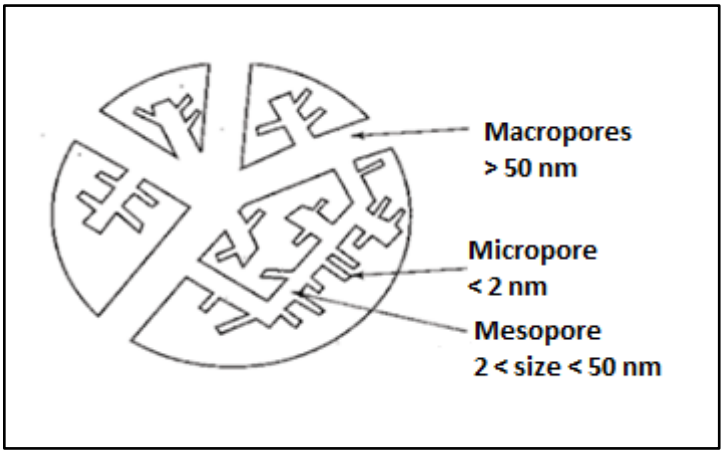

Fig. 1.2: Schematic of types of pore size

SC energy density is usually enhanced by increasing voltage window, which depends on SSA and PSD. Also, it depends on size of electrolyte ions, mobility, redistribution, arrangement of the ions and transporting ions through pores into surface electrode materials. Increasing SC power density can be established by, decreasing ESR of the SC as possible as we can [7, 9, 19].

By optimizing the appropriate properties of materials and ion transporting electrolyte, the energy and power densities can then be optimized to be higher in their application in devices [1]. Therefore, SCs can be used in many industrial and engineering fields; such as electric vehicles, memory devices, automobile and smart clothes [1, 15, 18].

1.2: Components of SCs

SCs consist of three essential components: two electrodes, electrolyte and separator [2, 17, 19] as shown in figure 1.3 [21]. Carbon and/or metal oxide materials are used as electrodes [6, 7, 17]. Aqueous or organic electrolyte can be used with separator between the electrodes [17, 19].

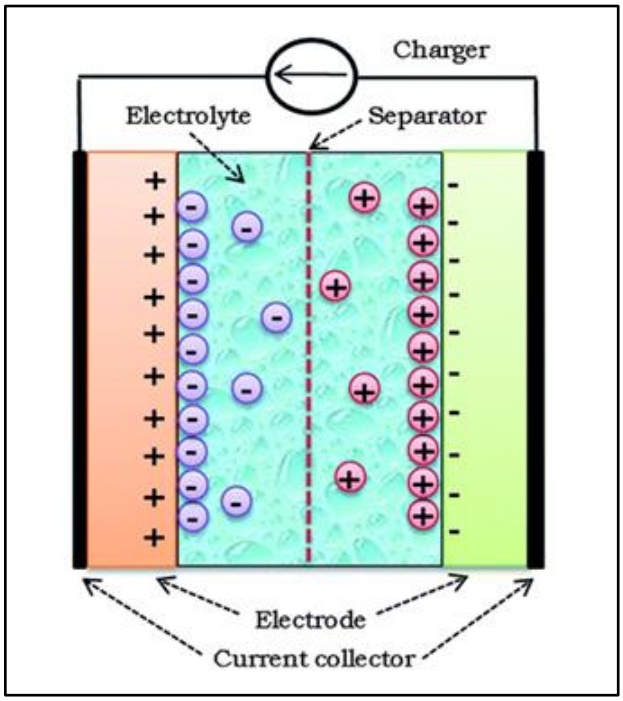

Fig. 1.3: Schematic representation of SCs

1.2.1: Electrodes

The electrode is one of the important components of SCs which effect the electrochemical properties of SC [16]. Mass, thickness, porosity and type of electrode are factors that must be taken into consideration for choosing the best electrode, which can give high energy and power densities [16, 18]. Carbon and/ or metal oxide materials and conducting polymers can be used as SC electrodes. Polymers are used for binding carbon particles together [3]. Such as poly(tetra-fluoroethylene) (PTFE), polyvynilidene chloride (PVDC) and polyvynilidene fluoride (PVDF) [3, 18]. However, if polymer ratio is increased, the capacitance decreases, because polymers block the pores, decrease micropores, mesopores and increase the external surface area around the pores which cause decrease the performance of SC. So, the amount of polymers should be optimized to be as low as possible [3, 22].

1.2.1.1: Carbon materials

Carbon materials are usually used as electrodes due to its low cost, abundant, high porosity, long cycling life, low resistance, high SSA (up to 3000 m^2/g) and high pore volume (about 1.6 cm^3/g). CO_2 or KOH treatment are used to increase SSA by opening closed and clogged pores [3, 17, 19].

Active carbon (AC), carbon nanofibers (CNFs), carbon nanotubes (CNTs), graphene, graphite and graphene nanoplateletes (GNPs) are examples of carbon materials which are used as SC electrodes [3, 12, 23].

Carbon electrode can give a high specific capacitance such as the C_S for AC is 334 F/g, power and energy densities can be achieved up to 450 W/kg and 18.1 Wh/kg, respectively, and its ESR is about 3.72 Ω [18].

1.2.1.2: Metal oxide materials

Metal oxides such as manganese oxide (MnO_2), graphene oxide and nickel oxide (NiO_2) are used as SC electrodes. This is because of their variety in surface structure, they have many transition states, so they can reach high energy and capacitance [9, 24, 25]. For example, the C_S of MnO_2 can be achieved to 261 F/g. However, metal oxides are expensive, they have low charge/discharge current density rate (0.5 mA/cm^2 for MnO_2) and they are suitable for aqueous electrolytes only [17, 19].

1.2.1.3: Conducting polymers

P and n- dopable (3-arylthiopene), p-doped poly (pyrrole), poly (3-methylthiophene) (pMet), polyaniline and polythiophene are examples for conducting polymers [17, 26]. This type of electrodes can give high capacitance density such as the C_S of p and n-doped pMet is 220, 165 F/g, respectively [26]. Due to its molecular structure, flexibility and low density it can be used at high operating voltage up to 3 V, and it gives high energy density. However, its conductivity is low so it has limited power density.

Moreover, its stability decreases at long cycling due to swelling and shrinking [9, 17].

1.2.2: Electrolyte

The second component of SCs is the electrolyte, which can be aqueous or organic [9, 19]. Two criteria are used to determine the kind of the electrolyte: voltage window and ionic conductivity. Voltage window determines energy density and ionic conductivity determines power density [19].

Aqueous electrolytes can be acid or alkali such as Potassium Hydroxide (KOH), Sodium Sulfate (Na_2SO_4) and Sulfuric Acid (H_2SO_4) [17]. They can be easy manipulated, low cost and environmentally friendly. Also, they have small resistance, high conductivity up to 1 S/cm (conductivity of H_2SO_4 and KOH is 0.8, 0.6 S/cm, respectively) [17, 27]. So they achieve high power density, but because its voltage window is limited to 1 volt, the energy density is reduced [17, 19].

Organic electrolytes, such as polymers, propylene carbonate and acetonitrile-based ones can achieve high voltage window (2- 3 V) depending on impurities of components. However, high voltage window can cause corrosion of carbon electrodes and separators [17]. An example of using organic electrolytes in carbon electrodes, SC was found to have C_S in the range of 100 to 150 F/g [19]. Other example when using activated carbon as electrode and gel polymer as electrolyte, energy density in the

range of 11- 17 Wh/kg was achieved. On the other hand, organic electrolyte solubility is low, so conductivity is also low (0.02 S/cm), which leads to reduction in power density [17, 19, 27].

1.2.3: Separator

The third component of SCs is the separator. Which is placed between the two electrodes to prevent electrical contact. Glass fiber separator can be used due to its high porosity and very thin, so the ions can pass through quickly and easily from electrolyte to the electrodes. Also, its resistance is very low. However, if the voltage window is very high, this causes corrosion of glass fiber separator [7, 27].

1.3: Principle and mechanism

The mechanism of how SCs are working depends on the storage charges in the pores on the surface of the electrodes. When SC is connected to the power supply, it will be polarized. The ions in the electrolyte will be diffused towards the opposite sign electrode. During diffusion, the ions penetrate the pores in the electrode material and electrode/electrolyte interface is formed [19] as shown in figure 1.4 [28].

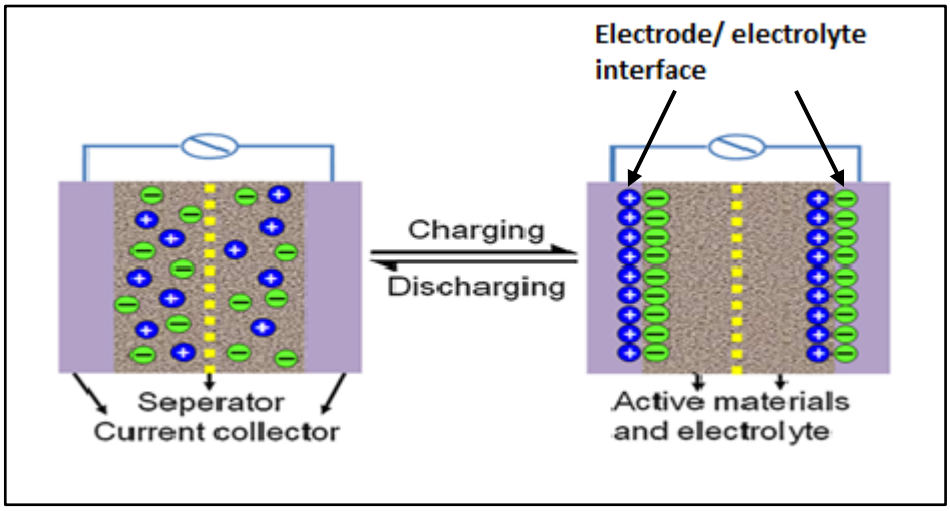

Fig. 1.4: Schematic of mechanism of how SCs work

There are three models describe the potential of ions between electrolyte and electrodes. The first model is Helmholtz model as shown in figure 1.5 (a) [29]. The potential is decreasing linearly with the distance between ions and electrodes. But this model does not take into account the diffusion of ions and the influence of the voltage on the capacitance, because the interaction of dipole moment between solvent and electrodes have not been obtained [19, 30].

The second model is Gouy and Chapman model which is shown in figure 1.5 (b) [29]. Poisson equation and Boltzmann distribution function are used in this model for calculations. In this model, the potential is decreased exponentially in the diffuse layer, which is a layer in the electrolyte where the ions are diffused in. But Gouy and Chapman model cannot be used in high charge double layer. Because the ions behave as point charges with no restrictions on potential, which is not true [6, 19, 30].

The third model is Stern model which is shown in figure 1.5 (c) [29]. This model combines Helmholtz and Gouy- Chapman models together. Which demonstrates the movement of ions in diffusion layer. Also it describes the accumulation of charges in compact layer. Two regions are obtained in compact layer; inner region where the ions are specifically adsorbed and outer region where the ions are non- specifically adsorbed.

Inner Helmholtz plane (IHP) and outer Helmholtz plane (OHP) are the planes which are used for distinguishing the two regions from each other. IHP exists near the specifically adsorbed anions, while OHP is at non-specifically adsorbed cations [6, 30].

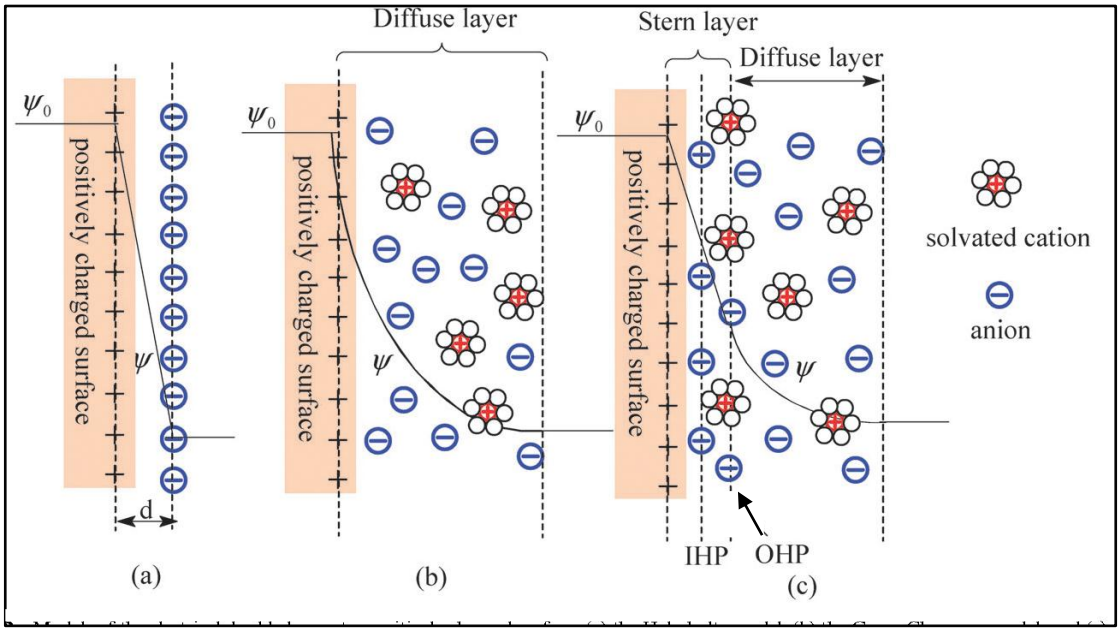

Fig. 1.5: Models for potential of ions between electrodes and electrolytes, (**a)** Helmholtz, (**b)** Gouy- Chapman and **(c)** Stern models.

1.4: Types of SCs

According to the way of charge storage, SCs can be classified into three types: electric double layer capacitors (EDLCs), pseudocapacitors and hybrid capacitors [6, 7, 14]. Figure 1.6 [31] shows the first two types of SCs.

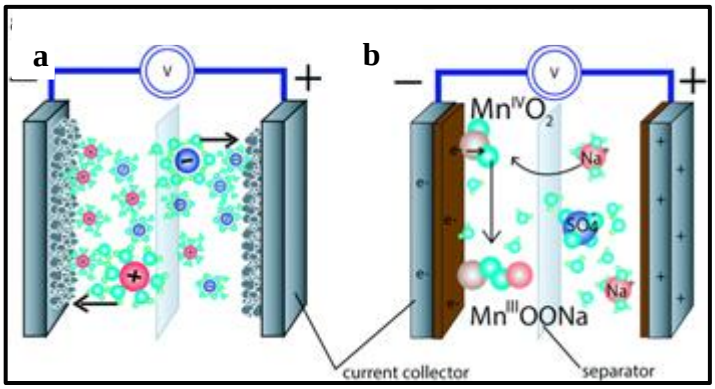

Fig. 1.6: Schematic of types of SCs: (**a**) EDLC, (**b**) Pseudocapacitor.

1.4.1: Electric double layer capacitors (EDLCs)

Carbon materials are used as electrode in this kind of SCs. EDLCs store energy electrostatically by adsorption the ions from electrolyte at electrode/electrolyte interface with no charge transfer between them [2]. The thickness of the double layer is about few nanometers which depends on the concentration and size of the ions in the electrolyte [17]. For good performance the size of the ions must match the size of pores on the surface of the electrode. So the ions aligned vertically in the pores. Then more ions can occupy it which cause an increase in the capacitance [19].

EDLCs can achieve high power density up to 15 KW/kg. But the energy density is about (5-8 Wh/kg) [11, 32].

1.4.2: Pseudocapacitors

Pseudocapacitors store energy electrochemically by oxidation/reduction reaction (Faradic effect) [19]. They are classified into three types: underpotential deposition, redox pseudocapacitance and intercalation pseudocapacitance. A monolayer is formed from adsorbed ions on the surface of the electrode as shown in figure 1.7 (a) [32]. This is called underpotential deposition. When the ions are adsorbed on and near the surface with charge transfer as shown in figure 1.7 (b), it is called the redox pseudocapacitance. But when the adsorbed ions are intercalated into tunnels or layers, with charge transfer and no phase change, then it is the intercalation pseudocapacitance (figure 1.7 (c)) [32].

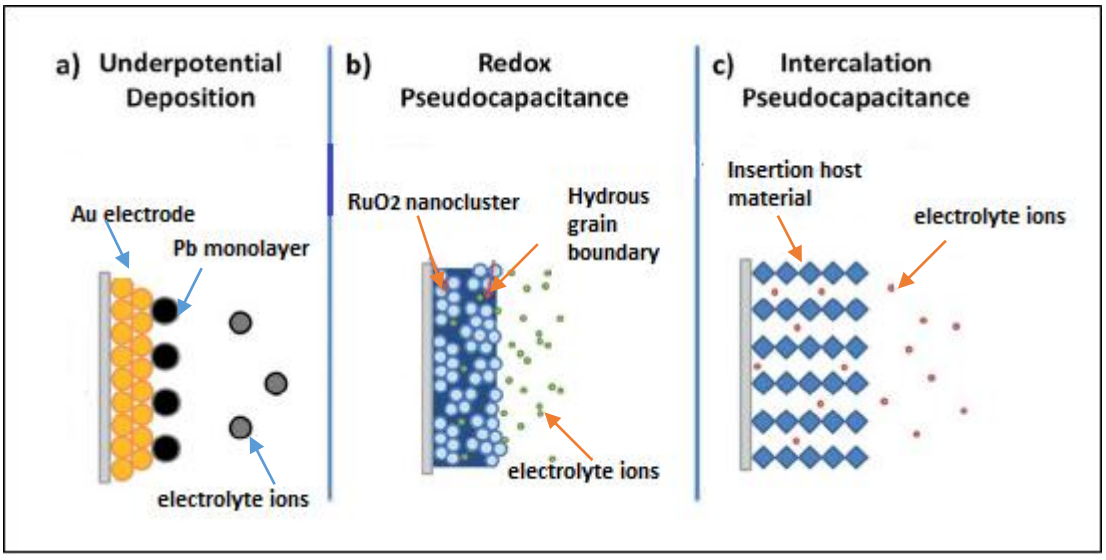

Fig.1.7: Types of pseudocapacitors.

Metal oxide or conducting polymers are used as electrodes for pseudocapacitors. Such as NiO, MnO_2, Co_3O_4, V_2O_5, Fe_3O_4, RuO_2, pMET and p- doped polypyrrole [9, 26]. This kind of SCs can achieve a very high energy density due to its high charge/ discharge time; which is in the range of 10 seconds to 10 minutes [32]. Also its C_S is very high. For example, C_S of MnO_2 is 261 F/g [25], and for RuO_2 C_S can be reached to 1360 F/g [9]. However, it is too expensive and it has low conductivity. The conductivity of MnO_2 is in the range of (10^{-7}- 10^{-3} S/cm) [32]. However, its power density is reduced relative to EDLCs due its high resistance and large diffusion distance [11].

1.4.3: Hybrid capacitors

The kind which combine both EDLCs and pseudocapacitors is called hybrid capacitors. Which can store energy both electrostatically and electrochemically [19]. Hybrid capacitors are used to treat the low energy density and C_S of EDLCs. And minimize the resistance of pseudocapacitors [9, 10]. Also, increase voltage window up to 2 V of aqueous electrolytes [33].

Hybrid capacitors are using carbon materials/ transition metal oxides composite or asymmetric materials as electrodes [9, 10]. Such as AC/ MnO_2, AC/ NiO, AC/ $Li_2Mn_4O_9$, CNF/ MnO_2 and AC/ a-MnO_2.nH_2O. For good performance the concentration and size of particles of the mixture of the materials must match each other. So the energy density can be enhanced [9].

Figure 1.8 [9] shows hybrid capacitor preparation. First type is prepared by asymmetric electrodes. One of the electrodes is battery- type (pseudocapacitive materials) and the other electrode is capacitor- type (carbon materials). The second type of preparation is from two symmetric composite materials electrodes.

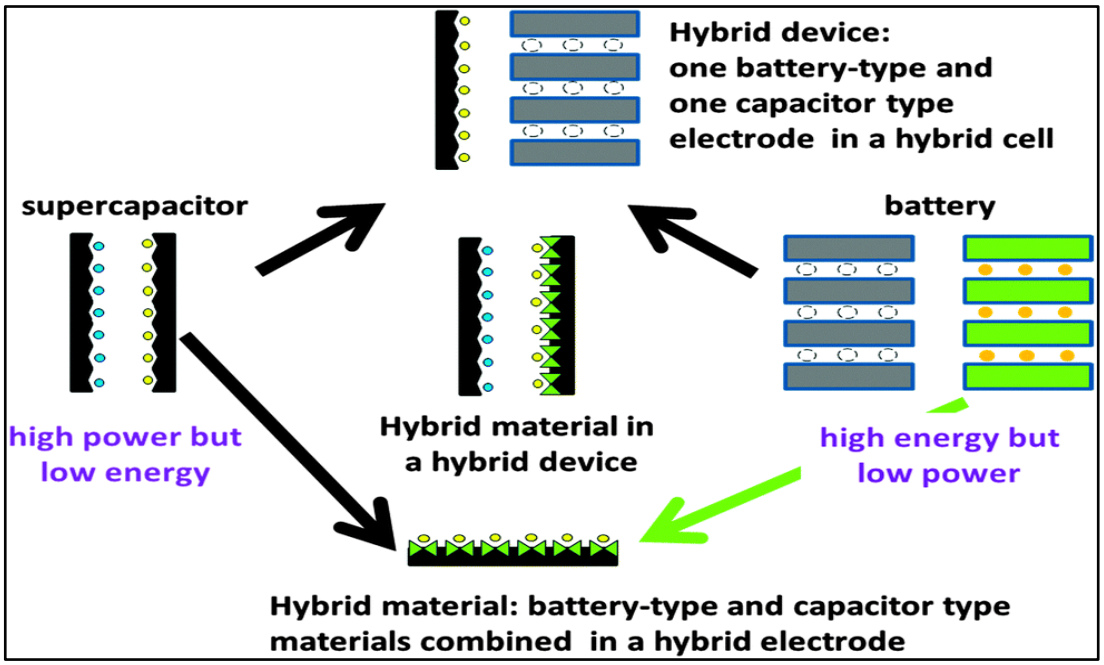

Fig. 1.8: Schematic of hybrid supercapacitors

The C_S of CNF/ MnO_2 electrode with high SSA (240 m^2/g) is 303 F/g, and energy density is reached to 72.4 Wh/kg [25]. Also, the energy density of AC/ a-$MnO_2.nH_2O$ as electrodes is 28.8 Wh/kg at 0.25 A/g [33].

1.5: Literature Survey

Many applications and devices depend on the development of SCs. So many reports and researches took attention on the parameters that affect the efficiency of SCs.

A. Nishino [34] has studied the capacitance of conventional capacitors which is in the range of (0.1- 1 μF). Becker [35] has developed the principle of EDLCs. Then Sohio group [36] have used high area carbon powder material with salt electrolyte. The C_S for the best carbon materials as electrodes is in the range of 150 F/g [32]. In 1952, the influence of electrolyte at electrode surface on the performance of SCs was determined [10]. Nakamura et al. [37] have discussed the effect of surface functional groups containing oxygen on the stability of carbon electrodes in SC by using organic electrolyte. They found that, the stability increases with oxygen content when carbon was used as anode and decreases when it is used as cathode. Also, Demarconnay et al. [38] have observed the symmetric carbon/ carbon SC, in neutral Na_2SO_4 aqueous electrolyte, has a stable cell voltage window as high as 1.6 V. V. Ganesh et al. [1] have studied the symmetric and asymmetric SCs by using high surface area porous nickel and AC. In that study the C_S for single electrode for nickel is 473 F/g. X. Sun et al. [39] have done a comparative study by using AC as electrodes in Li_2SO_4 and KOH aqueous electrolyte, the C_S was found in Li_2SO_4 to be 80% higher than KOH electrolyte.

In 1889 CNFs had excellence as filaments produced from gases which include carbons. Then CNFs have attention from researchers in 1950 after manufacturing electron microscope analyser [40]. In 1970s, A. Oberline et al. [41] had prepared CNF from benzene and hydrogen at 1100° C. They found that CNFs have internal hollow tubes with diameter from 20 to 500 A°. Until 2005, new challenge was faced to develop SCs of high C_S by enhancing mesoporous carbons with high SSA [10].

A. Daraghmeh et al. [3] have also studied the concentration of binder and pressure on the performance of CNF, in their paper, ESR value was found to increase with increasing the concentration of polymers (from 0.3 to 1.9 Ω) and to decrease with increasing pressure. Also, the value of C_S was found about 80 F/g for the lowest concentration of polymer. Also, A. Daraghmeh et al. [25] did another research on the flexibility of high dense CNFs in different concentrations of KOH electrolyte. The C_S value was found for 9M KOH to be 38 F/g at scan rate 5 mV/s. Moreover, A. Daraghmeh [18] did a comparison study between AC and CNF, in this study CNF has achieved 1860 W/kg power density which is higher than the power density of AC (450 W/kg) due to its low ESR (0.28 Ω) relative to AC. In addition, M. Seo et al. [42] have done a comparative study between CNFs and activated carbon nanofibers (ACNFs), the average diameter was decreased by activation from 350 to 250 nm, and the SSA was increased by activation from 240 to 1250 m^2/g so the C_S of CNFs can be enhanced by activation. Moreover, Wang et al. [43] have calculated

Raman shifts via Raman spectroscopy and found that the Raman shift is in the range of 1050 to 2000 cm^{-1}.

J. Sun et al. [44] have improved electric conductivity of CNFs by fluorinated multiple wall CNT (MWCNT) which is achieved to 27 S/cm. M. Raimondo et al [45] have also studied electrical conductivity of CNFs. They found that conductivity and permittivity depend on frequency which are increased after certain value. They also found that permittivity is exponentially dependent on carbon nanofiller content. The thermal conductivity of CNFs was improved by A. Askounis et al. [46], who found that thermal conductivity of modified CNF by MWCNT is larger than CNFs and less than CNTs due to the changing in wall structure of CNFs.

F. Hoshi et al. [47] had studied the binding energy of aligned CNF which was deposited on Si substrate. The binding energy was 284.6 eV which indicates sp^2 carbon structure with < 5% oxygen. Also, B. Kumar et al. [48] reported the catalytic ability polyacrylonitrile (PAN)- based heteroatomic carbon nanofibers for carbon dioxide reduction into carbon monoxide, via a metal- free and renewable route. The binding energy was 400 eV which indicates nitrogen presence, and 284, 284.8, 286 and 287.8 eV which correspond to C─C, C═C, C─N and O═C─N, respectively.

Also, many researches are concerned about graphene, which is two dimensional carbon monolayer. In fact, graphene uses as electrode material due to its light weight, high electrical and thermal conductivity, high chemical stability and has a very high SSA (2675 m^2/g) that gives C_S in

the range of (100- 250 F/g) [7, 32]. Stoller et al. [16] have studied the reduced graphene oxide as electrodes, the C_S was found 135 F/g with aqueous electrolyte and 99 F/g with organic electrolyte. Moreover, the C_S for graphene nanosheets is found (38- 264 F/g), which depends on the preparation methods, SSA, number of layers and the kind of the electrolyte [14].

Many studies suggested the use of GNPs to enhance SSA and surface roughness [49]. M. Beidaghi et al. [14] have studied GNPs with SSA (600-750 m^2/g), the C_S for 1 μm and 6 μm thickness was found 52, 49 F/g, respectively at scan rate 0.1 V/s. And C_S by using 1M Na_2SO_4 for 1 μm and 6 μm was 55, 53 F/g respectively at 1 A/g. They also found the specific energy to be 2.93 Wh/kg. M. K. Singh et al. [50] have studied EDLC with GNPs as electrodes and gel polymer electrolyte, the C_S value was about 57 F/g evaluated at 10 mHz, and ESR was 170 $\Omega.cm^2$ at 0.5 A/g in charge/ discharge process.

Bonso et al. [51] have also demonstrated GNPs/ V_2O_5 composite as SC electrodes, the C_S was 35 F/g with aqueous electrolyte and 226 F/g with organic electrolyte. A. Singh et al. [12] have studied asymmetric SCs by using MCNT/ NiO_2 and GNPs as electrodes, the C_S was 181 F/g at 1 A/g and the maximum energy density was 49 Wh/kg. They also found that at 10 A/g the power density achieved 7000 W/kg at energy density 17 Wh/kg. Also, Ch. Shi et al. [23] have discussed high porous carbon with

GNP, the C_S was evaluated in 2M KOH and 1M Na_2SO_4 at 1 A/g which was 329, 311 F/g, respectively.

Huang et al. [52] has improved the electric conductivity of GNPs which is reached to (4.3×10^4 S/cm). Then Scida [53] has manufactured GNP based on antenna to enhance the conductivity of GNPs ($\sigma \approx 10^5$ S/cm). Moreover, S. Biswas et al [54] have enhanced the electrical conductivity of liquid crystalline polymer (LCP) by adding 5% GNPs to LCP, and the measured conductivity was 4.5×10^{-4} S/cm. S. Kim et al [55] has used composite of 20% GNPs filler GNPs and carbon black (CB) to study thermal conductivity and obtained 1.98 W/mK.

Sh. Ding et al. [56] used polypyrrole (PPy) and GNP composite as SC electrodes. SSA was 136.5 m^2/g, C_S achieved 285 F/g. Also, binding energy was 284.7, 285.6, 286.7 and 288.3 eV which is related to C─C, C─N, C─O and C═O, respectively.

1.6: Why carbon nanofibers and graphene nanoplateletes have been used as supercapacitor electrodes?

The performance of SCs depend on the electrode materials and on type of the electrolyte. Researches are focusing on increasing energy density of SCs by increasing C_S. So, enhancing the morphological properties of the electrode materials will give high energy density. At the same time limiting the value of ESR to keep higher power density [16].

Many researches and papers are focused on CNF as SC electrodes. Due to its properties: good stability, high length to diameter ratio, good thermal and electrical conductivities (ESR = 0.3 Ω), SSA and flexibility. CNF has sp^2 linear filament like cylindrical structure with graphene layers as cups or cones as shown in figure 1.9 [18, 57, 58, 59] with diameter in the range of (100- 350 nm) [3, 25, 60].

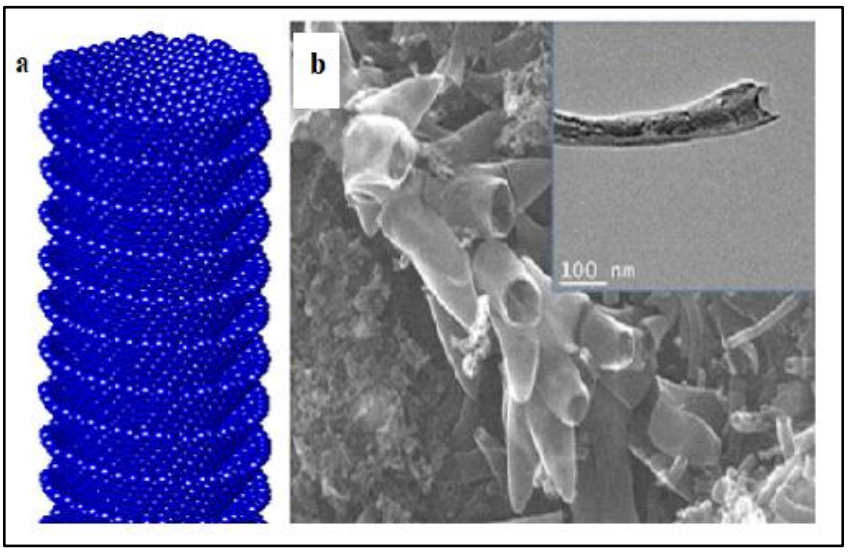

Fig. 1.9: CNF structure (**a**) schematic of the shape and (**b**) CNF structure by TEM.

The SSA of CNF can be achieved up to 973.4 m^2/g; according to the preparation method [60]. Without using polymers SSA of CNF is 165 m^2/g. The highest C_S of CNF in 6M KOH electrolyte by using 10 wt% of PVDF and 1783 MPa is 96 F/g. Which gives a very high power density (24502 W/kg) and energy density to be consistent 6.8 Wh/kg [3, 7, 25]. Bonso et al. [61] have treated CNF by electrospun and obtained SSA value of 11662 m^2/g, which gives high C_S (120 F/g) at scan rate 10 mV/s by

using liquid ionic electrolyte. So the energy density increased to 60 Wh/kg at power density of 1700 W/kg.

CNFs have uniform distribution of mesoporous [62]. Many researches proved that such as the study by A. Daraghmeh et al. [18] they found that 59% of the total pore volume is meso- volume, which is about 0.2 cm^3/g, which contributes to the values of C_S.

Furthermore, GNPs consider as a promising candidate for preparing electrodes, because GNPs are thermal conductive polymer which have a very high SSA in the range of (600- 750 m^2/g) [14, 63] with thickness in the range of (0.34 to 100 nm), light weight, flexibility, and its resistance is very low [12, 57]. Also, GNPs have high porosity, which has a planar structure with few layers of sp^2 bounded carbons to form 2D material with nanometer thickness [9, 23, 50, 58] as shown in figure 1.10 [64]. So, GNPs can increase stability, stiffness, thermal and electrical conductivity of SCs [49].

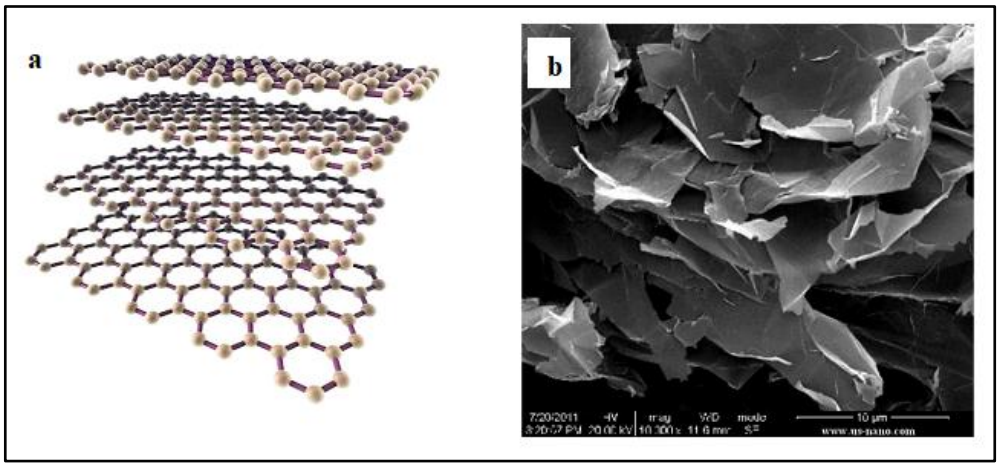

Fig. 1.10: GNP structure (**a**) schematic of shape and (**b**) GNP structure by GNP.

GNPs have demonstrated in 1M H_2SO_4 electrolyte. The C_S is 53 F/g, and the achieved energy and power densities were 2.93 Wh/kg and 75.46 KW/kg, respectively. However, GNP's energy density has increased up to 8.2 Wh/kg with using gel polymer electrolyte, but the power density is less than using aqueous electrolyte (16.4 KW/kg) [14, 50].

From the previous researches, we expected using CNF/GNP composite as SC electrodes will give higher C_S, conductivity, power and energy densities and lower ESR.

1.7: Objectives of this thesis

The general aim of this study is to enhance the efficiency of SCs, which is prepared by CNF/GNP composite as electrodes. The improvement is obtained by increasing power and energy densities. The energy density (specific energy) can be increased by increasing C_S. And the power density (specific power) can be increased by decreasing ESR. This can be done by:

1. Studying the effect of the concentration of CNF/GNP composite as SC electrodes by using 1 M KOH electrolyte.

2. Studying C_S, ESR, power and energy densities for the electrodes by using potentiostate in three different ways: cyclic voltammetry (CV), galvanostatic charge/ discharge (GCD) and electrochemical impedance spectroscopy (EIS).

3. Studying surface and structural morphology of the electrode materials by using scanning electron microscope (SEM) and transmission electron microscope (TEM).

4. Studying SSA and PSD by using Brunauer- Emmett- Teller (BET), Barrett- Joyner- Halenda (BJH), Harkins- Jura and micropore (MP) methods.

5. Comparison between the prepared electrodes to determine the best concentration which give the highest power and energy densities.

1.8: Thesis Structure

Chapter One: Introduction

This chapter explains SCs, its components, types and principle of how SCs are working. In addition, literature survey of some studies and reports about CNFs and GNPs are obtained in this chapter. Properties of CNFs and GNPs are presented to demonstrate why these two materials are used in the experimental part of this thesis. Finally, the objectives of this thesis are explained in the final section of this chapter.

Chapter Two: Theory

In this chapter, theories are presented about numerous methods to calculate the electrochemical characterization by CV, GCD and EIS methods. Then, in the second section of this chapter different techniques are investigated to

obtain SSA by BET method and PSD by BJH, Harkins- Jura and MP methods.

Chapter Three: Experimental

Materials, devices, way of preparation of electrodes and electrolyte which are used in the experiment are discussed in this chapter. Then, methodology of electrochemical calculations is provided. Finally, surface, morphology and pore texture measurements are classified in the final section of this chapter.

Chapter Four: Results and Discussion

This chapter discussed the structural behavior of CNF/ GNP composites with different concentrations by N_2 adsorption/ desorption isotherms, SEM and TEM. Also, physical properties are investigated and presented in the second section of in this chapter.

Chapter Five: Conclusion

In the final chapter of this thesis the basic results, properties of the prepared SCs are given and recommendations for enhancing this work in near future are suggested.

Chapter Two
Theory

The ability for storing energy in conventional capacitors depends on the amount of accumulated charges in each electrode when maintaining potential difference between them which is given by [65]:

$$q = C\,V \tag{2.1}$$

Where q is the charge on each electrode in coulomb (C), C is the capacitance in Farad (F) and V is the potential difference in volts (volt).

For parallel plate capacitor; $q = \sigma A$ and $V = \Sigma\, d$. Where σ is charge density (C/cm^2) and Σ is the electric field which is equal (σ/ε) by Gauss law. The capacitance is also a geometrical function, which depends on the dimension of the capacitor according to [17, 65]:

$$C = \varepsilon \left(\frac{A}{d}\right) = \varepsilon_r\, \varepsilon_0 \left(\frac{A}{d}\right) \tag{2.2}$$

Where ε_r is the dielectric permittivity constant of the dielectric material which indicates that the material not allow the electric field to pass through it, ε_0 is the permittivity of the free space ($8.854 * 10^{-12}$ F/m), A is the area (in m^2) and d is the thickness of the dielectric material (in m).

The energy stored in the electric field established between the two electrodes can be calculated using:

$$E = \frac{1}{2} C\,V^2 \tag{2.3}$$

Where E is the stored energy in Joules (J).

Equations (2.1) and (2.2) can also be used in the case of SCs to calculate energy density. Where q is the accumulated charge density on the electrode/ electrolyte interface, V is the operating voltage (voltage window), ε_r is the electrolyte permittivity, A is SSA and d is the effective distance (the distance between ions and pore surface of the electrode in the range of 5- 10 A°), which depends on the concentration and the permittivity of the electrolyte. The energy density, which is stored in SCs, is higher than that in the conventional capacitors because the electric field in the SC between the opposite charges at the electrode/ electrolyte interface can be achieved up to 10^6 V/cm [10, 17, 25, 65].

According to equation (2.2), two challenges are obtained for increasing C_S, which are increasing SSA and decreasing the effective distance. Therefore, developing the parameters which contribute to the behavior of SCs have a great interest to replace the known energy sources. Electrochemical, structural and surface characterizations are used to investigate the properties and behavior of SCs by different numerous methods and techniques [3, 15, 66].

2.1: Electrochemical characterization

The performance of SCs can be determined by discussing the electrochemical properties, which are C_S, E, P and ESR. Electrochemical

characterization can be studied by three different methods: CV, GCD and EIS [6- 8, 11].

2.1.1: Cyclic voltammetry (CV)

Electrochemical behavior of SCs can be investigated by CV method in the range of 0 to 1V for aqueous electrolytes, at different constant scan rates ($S = dV/dt$). The developed resulted current is due to sweeping the potential between the two electrodes. The resulting CV curve is the current against potential, where the current is a function of time, I(t). The shape of CV curve can determine the type and stability (cycling life) of SCs. EDLCs have a rectangular CV curve, while the pseudocapacitors have CV curve with peaks. An example of CV curves for EDLC and pseudocapacitor is shown in figure 2.1 [6- 8, 11, 67].

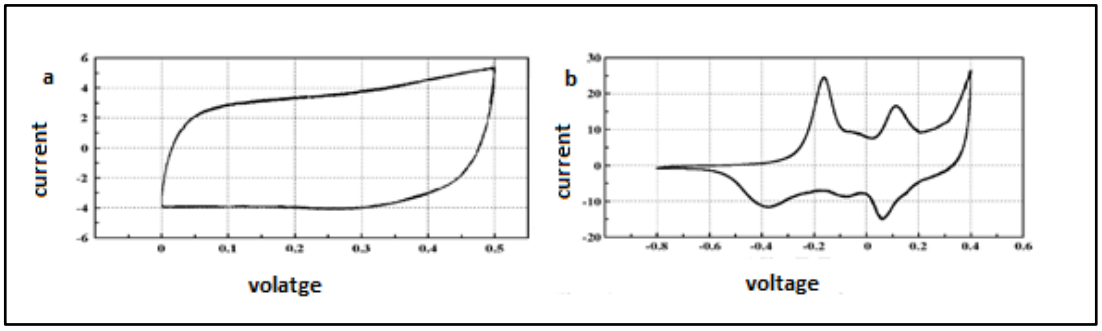

Fig. 2.1: Difference in CV curve for **(a)** EDLC, **(b)** Pseudocapacitor

For symmetric SC with electrodes equal masses, sizes, thickness and material, it is considered to have two equal capacitors in series, C_+ and C_- for positive and negative electrodes, respectively (figure 2.2 (a)). Each capacitor consists of diffuse capacitance (C_d) and compact capacitance (C_c)

according to Stern model as shown in figure 2.2 (b). Total capacitance and electrode capacitance can be found by [17, 19, 30]:

$$\frac{1}{C_{tot}} = \frac{1}{C_+} + \frac{1}{C_-} \tag{2.4}$$

$$\frac{1}{C^*} = \frac{1}{C_c} + \frac{1}{C_d} \tag{2.5}$$

Where C_{tot} is the total capacitance and C^* is the capacitance of the electrode. C_d contributes to the capacitance of the cell at low potential but it negligible if the electrolyte is concentrated [30].

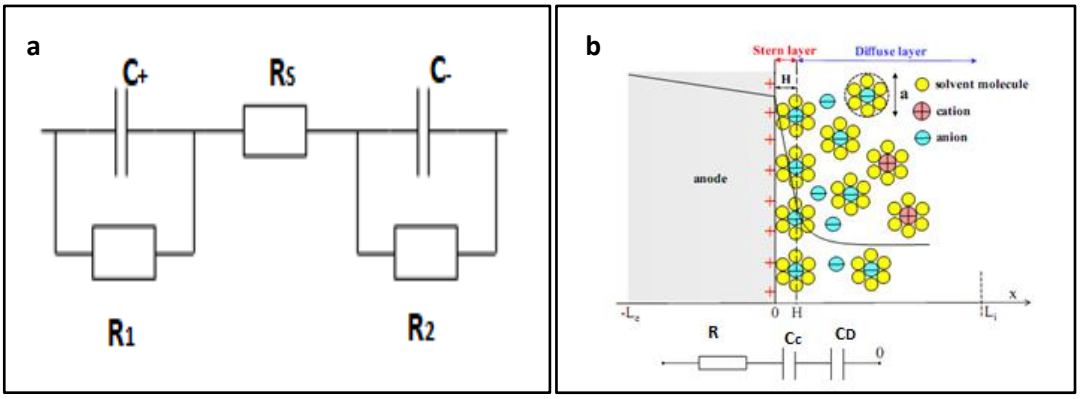

Fig. 2.2: (**a**) Schematic equivalent circuit for double layer capacitor and (**b**) compact and diffuse capacitances for one electrode according to Stern model .

Then the capacitance per unit mass for one electrode can be found by [3, 18, 25]:

$$C_S = \frac{4\,C}{m} \tag{2.6}$$

Where C_s is the specific capacitance (F/g), C is the measured capacitance and m is the active material of the electrodes in grams (g).

The measured capacitance (C) can be calculated by:

$$C = \frac{q_a + |q_c|}{\Delta V}, \quad (2.7)$$

where q_a and q_c are the anode and cathode charge densities, respectively, and ΔV is the voltage window (operating voltage) [18, 19].

Anode and cathode charges can be evaluated by the area under the curve of current density, I against time, t. According to:

$$\int dq = \int I\, dt \quad (2.8)$$

2.1.2: Galvanostatic charge/discharge (GCD)

Another way which is used for calculating electrochemical properties of SCs is GCD method. Different constant currents can be applied, between work and reference electrode, in this method to study the variation of potential with time for charge and discharge processes [6- 8, 11]. Typical charge/ discharge processes for SC is shown in figure 2.3 [68].

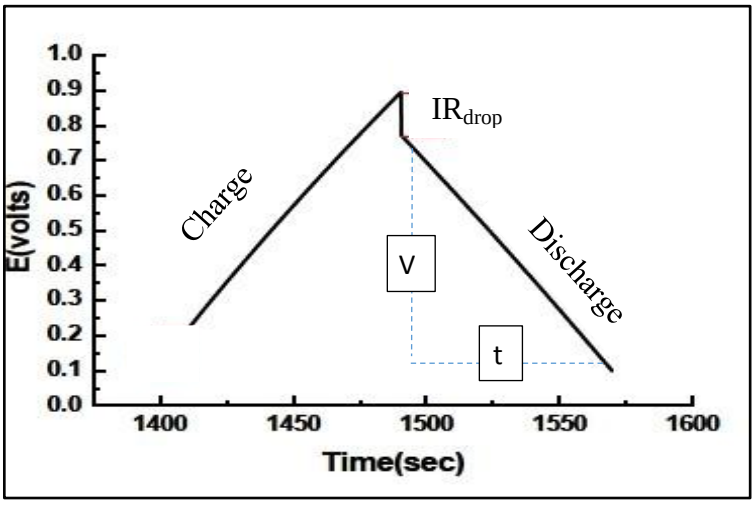

Fig. 2.3: Galvanostatic charge/ discharge curve for supercapacitor.

Equation (2.8) can be rewritten as following and substituting C from equation (2.6):

$$I = \frac{dq}{dt} = \frac{dq}{dV}\frac{dV}{dt} = C\frac{dV}{dt} = \frac{m_{tot}\,C_s}{4}\left(\frac{dV}{dt}\right) \quad (2.9)$$

C_S can be calculated for two electrodes by [1, 3, 18, 25]:

$$C_s = \frac{2\,I}{m\frac{dV}{dt}} \quad (2.10)$$

Where I is the discharge current (A), m is the mass of one electrode and $\frac{dV}{dt}$ is the slope of the final discharge process (in volt/sec).

GCD method is used for constructing Ragone plot. This plot represents power density against energy density. The power density (W/kg) is given by [18]:

$$P = \frac{I\,V}{m} \quad (2.11)$$

Where V is the potential difference excluding voltage drop ($V_{drop} = I\,R_{drop}$ represents the gap between charge/ discharge processes) and m is the mass of one electrode [3, 18, 25].

The energy density (Wh/kg) of one electrode is calculated by using [18]:

$$E = P\,t \quad (2.12)$$

Where t is the discharge time in seconds (s). To convert the unit of energy density from (J/kg) to (Wh/kg) multiply equation (2.12) by $\frac{1W.s.\ h}{3600\ s}$ [19].

The maximum power density for SC can be determined by:

$$P_{Max} = \frac{V^2}{4\,(ESR)\,m} \tag{2.13}$$

Where ESR for one electrode can be calculated from the slope of the plot of V_{drop} versus I).

From GCD the efficiency (η) of SC can be calculated from [69]:

$$\eta = \frac{\Delta t_d}{\Delta t_c} \tag{2.14}$$

Where Δt_d, Δt_c are discharge and charge times, respectively.

2.1.3: Electrochemical impedance spectroscopy (EIS)

The electrochemical characterization can also be investigated by EIS analysis, which is also called Nyquist plot. AC current is resulted with phase shift due to apply sinusoidal potential in the range of 100 KHz to 10 mHz [18]. The applied potential as a function of time (V_t) is given by [70]:

$$V_t = V_0\,Sin\,(\omega\,t) = V_0 e^{j\,\omega t} \tag{2.15}$$

Where V_0 is the amplitude of the signal and ω is the angular frequency ($\omega = 2\pi\,f$).

The resulted current as function of time (I_t) with phase shift (φ) is determined by [70]:

$$I_t = I_0\,Sin\,(\omega t + \varphi) = I_0\,e^{j(\omega t - \varphi)} \tag{2.16}$$

Where I_0 is the amplitude of the signal.

Then the ability to resist the flow of current is called the impedance (Z) which can be calculated according to:

$$Z = \frac{V_t}{I_t} = \frac{V_0 \, Sin\,(\omega t)}{I_0 \sin(\omega t + \varphi)} = Z_0 \frac{Sin\,(\omega t)}{Sin\,(\omega t + \varphi)} = Z_0 \, e^{j\varphi} \qquad (2.17)$$

According to equation (2.17), the impedance has real and imaginary parts. The relation between real and imaginary components of the impedance is called Nyquist plot, which is divided into three regions according to the frequency: high- frequency, low- frequency and Warburg regions [6, 7, 70]. Semi-circle was investigated in high-frequency region. And straight line in low-frequency region. Warburg region is the transition region between high and low regions which is occurred at 45^0 phase shift. Diffusion of the ions can be demonstrated at Warburg region. According to the variable of frequency values, SCs can behave as resistor ($Z = R$) at high-frequency region, and as capacitor ($Z = \frac{1}{j\,\omega\,C}$) at low-frequency region as shown in figure 2.4 [6- 12, 65, 70, 71].

The first x- intercept of the Nyquist plot at the highest frequency region represents the solution (electrolyte) resistance (R_S), which depends on the temperature, type and concentrations of the ions. However, the arc resistance represents the charge transfer resistance (R_{CT}), which is the resistance of the electrolyte access into the pores in the electrode surface. R_{CT} depends on the reaction products and the potential. The total resistance which represents the sum of the ionic resistance of the electrolyte, electric resistance of the electrodes, the interface resistance between electrodes and current resistance is called ESR [6,7, 23, 25, 70, 71].

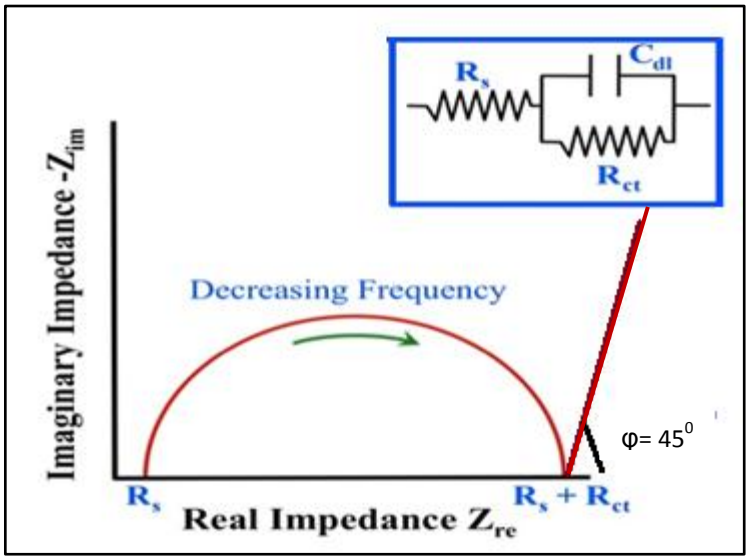

Fig. 2.4: Components of Nyquist plot for SC.

In this method, the specific capacitance of SC is calculated at low-frequency region ($Z = \frac{1}{j\,\omega\,C}$), by rewriting impedance formula [3, 18, 70]:

$$C_S = \frac{-4}{2\pi\, m\, f\, z``} \tag{2.18}$$

Where f is the lower frequency (Hz), $z``$ is the imaginary component of impedance at lower frequency (Ω) and m is the total mass.

One of the most important properties of SCs is time constant (τ) which represents how does SC respond. For small τ indicates fast response. τ depends on resistance and capacitance which can be evaluated by two ways as shown in the following equation [3, 19]:

$$\tau = (ESR)\, C = \frac{E}{2\, P} \tag{2.19}$$

Where ESR is the equivalent series resistance, C is the capacitance, P is the maximum power density and E is the energy density which can be

calculated from equation (2.3) where V is the voltage difference excluded voltage drop.

The time which is needed for transition from resistor to capacitor behavior is called relaxation time ($\tau_0 = 1/f_0$). Where f_0 is knee frequency which is the frequency at 45^0 phase angle [3].

2.2: Surface, morphology and structural characterization

The surface, morphology and structure of the electrode materials can be studied by different techniques. These techniques are important for explanation the electrochemical behavior and performance of SCs. The external surface morphology of the electrode materials can be studied using SEM. The internal surface of the materials is investigated by TEM. The SSA can be obtained by BET method. And the PSD are studied by BJH, Harkins- Jura and MP methods [6- 8, 11].

2.2.1: Brunauer- Emmett- Teller (BET), Barrett- Joyner- Halenda (BJH) methods

The external area of the electrode materials and the pore area are used to determine SSA by using BET analyzer. PSD, the area and volume of the pores can be determined by using BJH method. BET and BJH methods are based on nitrogen (N_2) multilayer adsorption/ desorption isotherms. Which is the amount of N_2 adsorbed or extracted at different pressures at certain temperature (77 K) [7, 8, 72].

The relation between the amount of N_2 adsorption/ desorption and relative pressure can be calculated from BET equation [73, 74].

$$\frac{1}{Q(\frac{P_0}{P}-1)} = \frac{1}{Q_m\, C} + \frac{C-1}{Q_m\, C}\,(\frac{P}{P_0}) \qquad (2.20)$$

Where $Q\left(\frac{P_0}{P}-1\right)$ is the amount of N_2 gas adsorbed, $\frac{P}{P_0}$ is the relative pressure (P is the pressure and P_0 is the saturation pressure), Q_m is the amount of adsorbed N_2 gas as monolayer and C is BET constant.

The SSA (in m^2/g) can be calculated from the linear plot of equation (2.20) between $\frac{1}{Q(\frac{P_0}{P}-1)}$ against $\frac{P}{P_0}$ as shown in figure 2.5 [74, 75]. The slope (s) is $\frac{C-1}{Q_m\, C}$ and the intercept (i) is $\frac{1}{Q_m C}$.

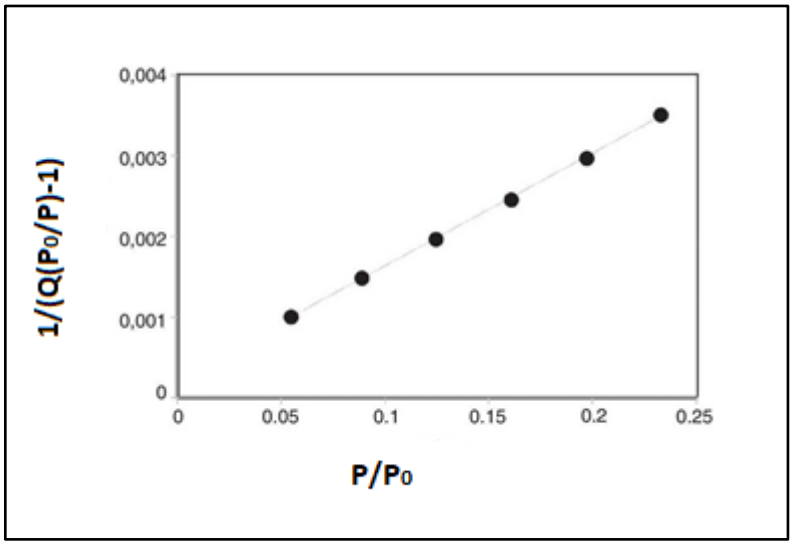

Fig. 2.5: BET plot.

So the quantity of adsorbate as monolayer can be calculated:

$$Q_m = \frac{1}{s+i} \qquad (2.21)$$

Then the total surface area (S_t) can be measured from:

$$S_t = \frac{Q_m N A_{cs}}{M} \quad (2.22)$$

Where N is Avogadro's number ($6.023 * 10^{23}$molecule/mole), A_{cs} is the cross sectional area of N_2 molecule (0.1620 nm^2) and M is the molecular weight of adsorbate (28 g/mol). The SSA can hence be measured by dividing equation (2.22) by mass.

PSD is distinguished by BJH, Harkins- Jura and MP methods. BJH is used to obtain the V_{tot}, meso and macro pore volumes and areas. But this method cannot distinguish micropores. Harkins- Jura method (t- plot) is used to investigate micro or meso pores and external area. While ultra-micro pores can be revealed by MP method which cannot detect meso and macro pores [3, 7, 18, 76].

BJH method is based on capillary condensation; where the gas is condensed to liquid in the pores at pressure less than saturation pressure. Area, volume and distribution of the pores can be described by explaining the equilibrium phase transition of desorption branch by using Kelvin equation [6- 8, 11].

The plot of the quantity of adsorbed gas against relative pressure, the desorption curve may overlay or on the left of adsorption curve due to the type of pores which is dominant in the material [7].

Adsorption isotherms are classified into six types according to IUPAC as shown in figure 2.6 [7]. In type I micropores are obtained with no or little external surface area. Type II shows macroporous or nonporous materials with unrestricted monolayer. Weak interaction between adsorbent and adsorbate which is shown in types III and V. And hysteresis loop is appeared in type IV due to complete filling and emptying mesopores with forming capillary condensation. In type VI peaks are observed relative to system and temperature with non- porous surface [7].

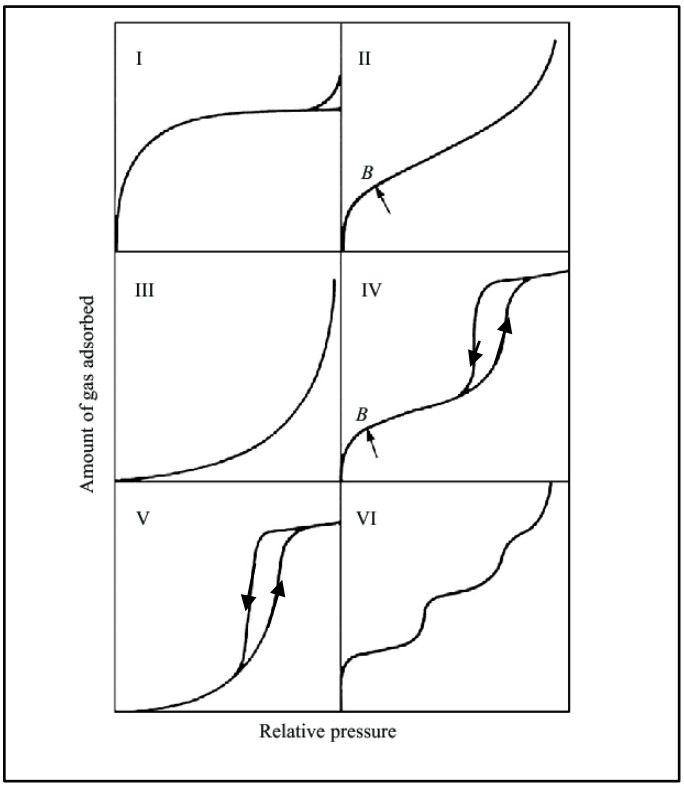

Fig. 2.6: Types of adsorption isotherms.

The total pore volume (in cm^3/ g) can be determined by the number of adsorbed nitrogen at maximum relative pressure of adsorption/ desorption isotherm (where $V_{tot} = V_{micro} + V_{meso} + V_{macro}$) [7, 18, 25].

Volume and area of meso and macro pores can be investigated by BJH desorption by calculating thickness (t) in Angstrom (A^0) of the adsorption layer at each relative pressure of N_2 isotherm [7, 74]:

$$t = 3.54 \left(- \frac{5}{\ln\left(\frac{P}{P_0}\right)} \right)^{\frac{1}{3}} \quad (2.23)$$

Incremental meso and macro volumes are calculated at each relative pressure depending on the quantity adsorbed of N_2, then the incremental meso and macro areas are calculated according to the following equation [7, 74, 77]:

$$V = S\, t \quad (2.24)$$

Where V and S are the volumes and areas, respectively of meso and macro pores.

For cylindrical pores, meso and macro pores can be distinguished according to the average pore diameter (in nm), which can be estimated as follows [77]:

$$\frac{V}{S} = \frac{\pi r^2 h}{2 \pi r h} = \frac{r}{2} \quad (2.25)$$

Where h is the pore depth and r is the pore radius ($r = \frac{d}{2}$). So, the average pore diameter estimates by:

$$d = 2\,r = \frac{4\,V}{S} \tag{2.26}$$

Then the volumes and areas of meso and macro pores estimated by cumulative volume and cumulative area.

Harkins and Jura method (t- plot) is used to evaluate meso area, micro area, micro volume and external area (S_{ext}) which represents the area around pores, by calculating statistical thickness by de Beor equation (equation 2.27) in the same range of relative pressure of adsorption/ desorption isotherm [76]:

$$t = \left(\frac{13.99}{0.034 - \log\left(\frac{P}{P_0}\right)}\right)^{\frac{1}{2}} \tag{2.27}$$

T- plot is the plot of quantity adsorbed of N_2 against thickness. If the relation between them is linear and the first linear fit of the plot of the quantity adsorbed and thickness ($V = (SSA)\,t$) at low pressure pass through the origin, then the mesopores are found in the material (figure 2.7 (a)). The slope of the first linear fit is SSA. Otherwise, if the first linear plot of the quantity adsorbed and thickness doesn't pass through the origin, then, the material consists of micropores, and the y- intercept equals micro volume as shown in figure 2.7 (b) [77- 79].

At high pressure, the adsorption occurs at external area because all pores are filled. The slope of the second linear fit of the plot ($V = S_{ext}\ t$) is equal S_{ext} for the two cases (figure 2.7 (c)). Then meso area in the first case and micro area in the second case can be calculated by subtracting external area from SSA as following [77- 79]:

$$S_{meso} = SSA - S_{ext} \tag{2.28}$$

$$S_{micro} = SSA - S_{ext} \tag{2.29}$$

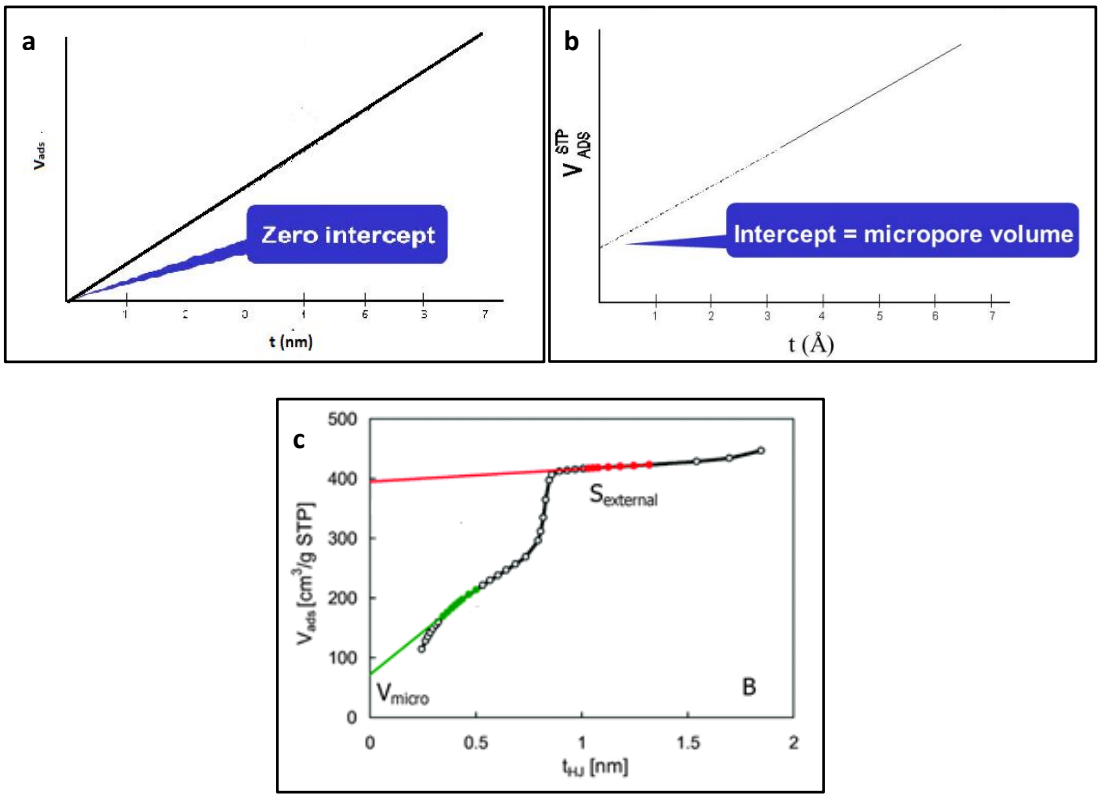

Fig. 2.7: T- plot in the presence of (**a**) mesopores, (**b**) micropores and (**c**) external area and micropores.

MP method is an extension of t- plot, which measures the distribution of micropores of size less than 0.7 nm (ultra- micropores). This type of micropores are calculated from the curvature of the t- plot near the origin

where the all micropores are filled. Also, MP method depends on evaluating thickness (equation 2.27) and the incremental volume to estimate the incremental area. Then the average pore hydraulic radius (in A^0) is measured by [79]:

$$r_k = \frac{v}{s} \tag{2.30}$$

Where V is the incremental volume and S is the incremental area of the ultra- micropore.

Chapter Three
Experimental

Preparation electrodes, electrolyte and studying the electrochemical behavior was done at An- Najah University. Structural and morphological characterization was obtained by Dr. Llorenc Servera at Barcelona University.

3.1: Materials and Setup devices

3.1.1: Materials

Materials which were used in this thesis are shown in table 3.1.

Table (3.1): Materials used in experiment

Material	**Purity**	**Source**
CNF	98.99%	Grupo Antolin
GNP	99.999%	Aldirch Chemistry
Glass fiber separator (MFV5)	99.99%	Alter- Lab
KOH		Frutarom LTD
Acetone (CH_3COCH_3)	99%	
Distilled water		

3.1.2: Setup devices

The experimental work was done in Advanced Material Science Lab- Physics Department and Heavy Instrumental Lab- Chemistry Department at An- Najah University. Surface morphology and pore characterization was measured at Barcelona University. The setup devices which were used in this thesis are listed in table 3.2. Figure 3.1 shows the devices used to study the electrochemical behavior at An- Najah University.

Table (3.2): Devices used in experiment

Devices	Model
Balance	AND HR- 200
Agate mortar	
Ultrasonic	Elmasonic S 10H
Oven	Ari j. levy
Magnetic Stirrer	LD RPM (666 839)
Swagelok cell	
Potentiostate	PGZ 402- Volta Lab
Press and molding machine	Shimadzu
SEM	Jeol J- 7100
TEM	Jeol 2011
BET analyzer	TriStar 3000 V6. 04A

Fig. 3.1: Devices used in experimental work: **(a)** press and molding machine, **(b)** balance, **(c)** magnetic stirrer, **(d**) oven, **(e)** ultrasonic, **(f)** Swagelok cell, **(g)** mortar and **(h)** potentiostate.

3.2: Preparation of electrodes by blade method

- Preparation the first sample; 10% GNP:

o Commercial CNF ($20 - 80$ nm) diameter, > 30 μm length, ($83\ m^2/g$) and ($10^{-2}\ \Omega.cm$) resistivity. And commercial GNP (Grade- C), 4- 5 layer of graphene, < 2 μm diameter and ($750\ m^2/g$) were used as electrode materials in this experiment.

o 90% wt. of CNFs with 10% wt. of GNPs was mixed in agate mortar.

o The slurry was mixed by using 20 ml acetone in ultrasonic (Elmasonic S 10H) for 20 min at 35 C^0.

o The slurry of the mixture was dried in oven (ari j. levy) for 60 min at 70 C^0 to have mixture powder.

o The powder was pressed by press and molding machine (Shimadzu) at 7 Ton; in Heavy Instrumental Lab- Chemistry Department.

o The prepared electrode discs were 0.07g, 13.7 mm diameter and 1.33 cm^2 area which are shown in figure 3.2.

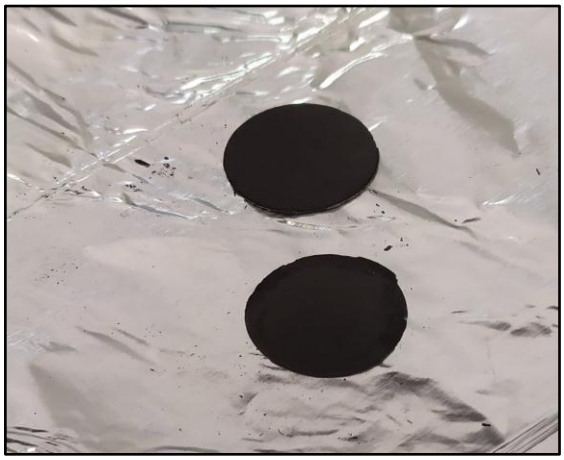

Fig. 3.2: Prepared electrode discs

- Doing same methodology of preparation with different concentrations of CNFs and GNPs:

  - Second sample; 30% GNP: 70% wt. CNFs with 30% wt. GNPs.
  - Third sample; 50% GNP: 50% wt. CNFs with 50% wt. GNPs.
  - Fourth sample; 70% GNP: 30% wt. CNFs with 70% wt. GNPs.
  - Fifth sample; 90% GNP: 10% wt. CNFs with 90% wt. GNPs.
  - Sixth sample; GNP: 95% wt. GNPs with 5% wt. polymer.

3.3: Preparation of aqueous electrolyte

1M KOH was used as aqueous electrolyte in this experiment. 5.61g of KOH (molar mass is 56.1 g/ mol with $K^{+1} = 0.152$ nm and $OH^{-1} = 0.11$ nm) was mixed with 100ml distilled water by using magnetic stirrer for 30 min as shown in figure 3.3.

Fig. 3.3: Preparation 1M KOH.

3.4: Methodology of electrochemical calculations

- Symmetric SC based on CNF/ GNP composites with different weight concentrations of GNP were used as electrodes.

- Glass fiber separator (MF V5- 110 mm size) was impressed in 1M KOH for few minutes until it was wet.

- Swagelok cell was used to assemble the components of SC together. The two symmetric electrodes and glass fiber separator with 1M KOH electrolyte between them was assembled as shown in figure 3.4.

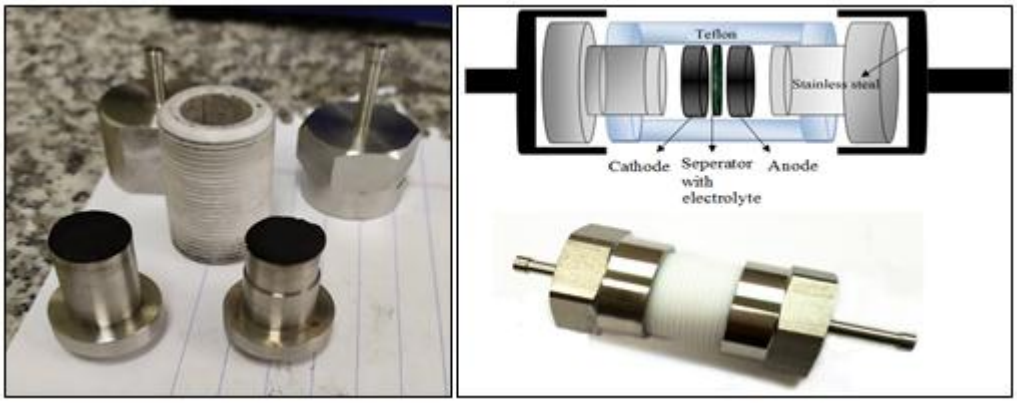

Fig. 3.4: Swagelok cell assembling

o Swagelok cell was connected to potentiostate (PGZ- 402). Work and sense leads were connected with each other, and auxiliary with reference leads were connected together as shown in figure 3.5.

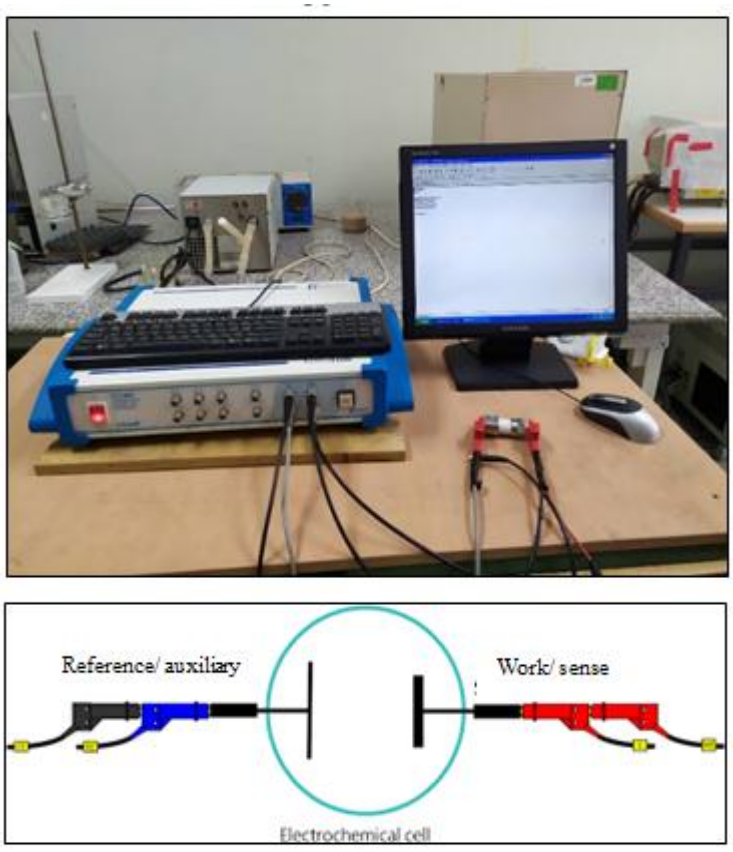

Fig. 3.5: Potentiostate connection.

- Potentiostate (PGZ- 402) was used to study the electrochemical characterization by three different methods: CV in the range of 0 to 1 volt at different constant scan rates (5, 10, 20, 50 and 100 mV/ s), GCD in the range of 0 to 1 volt at different constant currents (30, 50, 80, 100 and 130 mA) and EIS in the range of 100 KHz to 10 mHz at 20 mV AC sine wave amplitude.

- Comparison was made between the sample's results to determine the best concentration which gives the highest energy and power densities (the highest C_S and lowest ESR).

3.5: Surface and morphology texture measurements

Different techniques are used to determine texture, structural, crystalline feature, pore types and composition of the prepared materials which were used in the experimental part of this thesis.

3.5.1: Surface characterization

The SSA and PSD are determined by using N_2 adsorption. BET and BJH methods are used for calculating pore texture and evaluating the dominant pore volume in the testing sample.

3.5.1.1: BET analyzer and BJH method

The materials are exposed to N_2 gas of different pressures at certain temperature (77 K). At equilibrium, the amount of N_2 gas can be calculated by universal gas law. The total pore volume is evaluated at relative pressure

($\frac{P}{P_0} \approx 0.9924$). The SSA, pore areas and volumes, PSD and type of the pores can be obtained by BET, BJH, t- plot and MP methods.

BET analyzer (TriStar 3000 V6. 04A) which is shown in figure 3.6 is used to characterize SSA and PSD for CNF/ GNP composite.

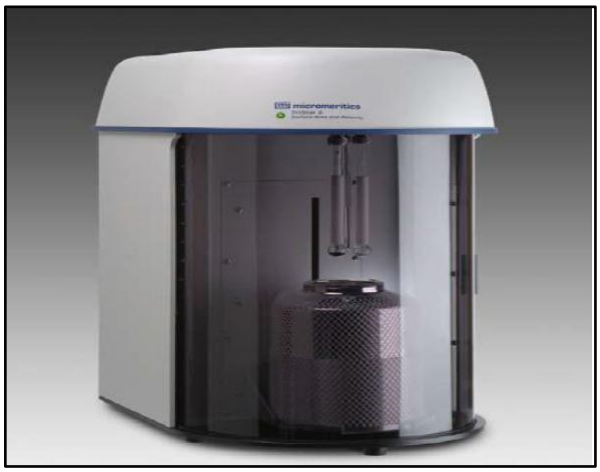

Fig. 3.6: BET analyzer (TriStar 3000 V6. 04A).

3.5.2: Morphology characterization

The external and internal morphology and composition structure of CNF/ GNP composite are examined by using SEM and TEM.

3.5.2.1: Scanning Electron Microscope (SEM)

The external morphology, topography (shape, feature and texture) and the composition of the materials can be studied by type of electron microscope, which is called SEM. Accelerated electrons are used in SEM to produce the image of the materials in raster scan pattern.

The accelerated electron beam is focused on the surface of the material by aperture. Which control the size of the beam which interact with the atoms on the surface of the sample. Then it emits secondary electrons which can be detected by detector. The number of the secondary electrons depends on the texture of the surface of the material.

In this thesis, the morphology of CNF/ GNP composite electrodes was measured by SEM (Jeol J- 7100) which is shown in figure 3.7.

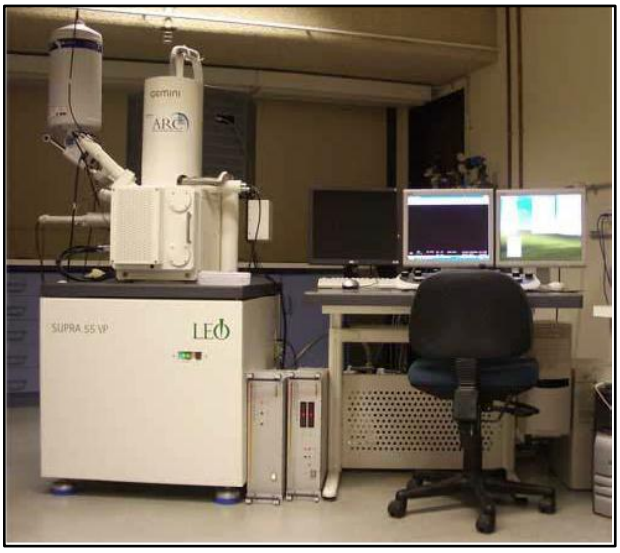

Fig. 3.7: SEM (Jeol J- 7100).

3.5.2.2: Transmission Electron Microscope (TEM)

The inner structure, morphology (texture, shape and size) and crystalline composition of the samples can be studied by TEM. Accelerated electrons are used in TEM to produce white and black image with high resolution.

The accelerated electron beam which is focused, hits the sample. Part of the beam is transmitted through the material. So the image which is formed consist of light and dark areas. The light portions are related to the transmitted electrons. While the dark ones represent the electrons which not pass through the sample.

TEM (Jeol 2011) is used in this thesis at accelerated voltage 20 KV to study the internal morphology of CNF/ GNP composite which is shown in figure 3.8.

Fig. 3.8: TEM (Jeol 2011).

Chapter Four

Results and Discussion

4.1: Electrochemical behavior

CNF/ GNP composite was tested as SC electrode materials, at different concentration of GNP (10%, 30%, 50%, 70% and 90%) by using 1M KOH as aqueous electrolyte. CV, GCD and EIS were used for evaluating C_S, E, P and ESR by using PGZ- 402 potentiostate.

4.1.1: Cyclic voltammetry behavior

The electrochemical behavior of CNF/ GNP composite was characterized by CV in the range of 0 to 1 volt at different constant scan rates (5, 10, 20, 50 and 100 mV/s). CV is the most appropriate method to recognize the capacitive characterization of the electrode materials.

CV curves of CNF/ GNP composites with GNP weight percent of 10%, 30%, 50%, 70% and 90% were shown in figure 4.1. At all scan rates, all samples had symmetrical shape CV curves. At low scan rate, CV curves presented semi- rectangular shape without any peak and with high reversibility charge and discharge processes, which indicates that the designed SCs in this experiment presents EDLC behavior [6- 8, 12, 55]. At high scan rates (50 mV/s and above), deviation from rectangular shape was observed. This was explained by the difficulty for ion species to enter all vacant sites in the electrode [80].

As also observed in figure 4.1, the current is directly proportional to the potential scan rate, which leads to have larger semi- rectangular area. The increasing of the current peak with high scan rates is due to the increasing the mobility of the ions, which caused high concentration that diffused near the electrode surface [81, 82].

The values of C_s for CNF/ GNP composite electrodes with different concentration of GNPs was calculated by using equations (2.6) and (2.7). Table 4.1 and figure 4.2 (deduced from the table) show C_S comparison of the samples for different scan rates.

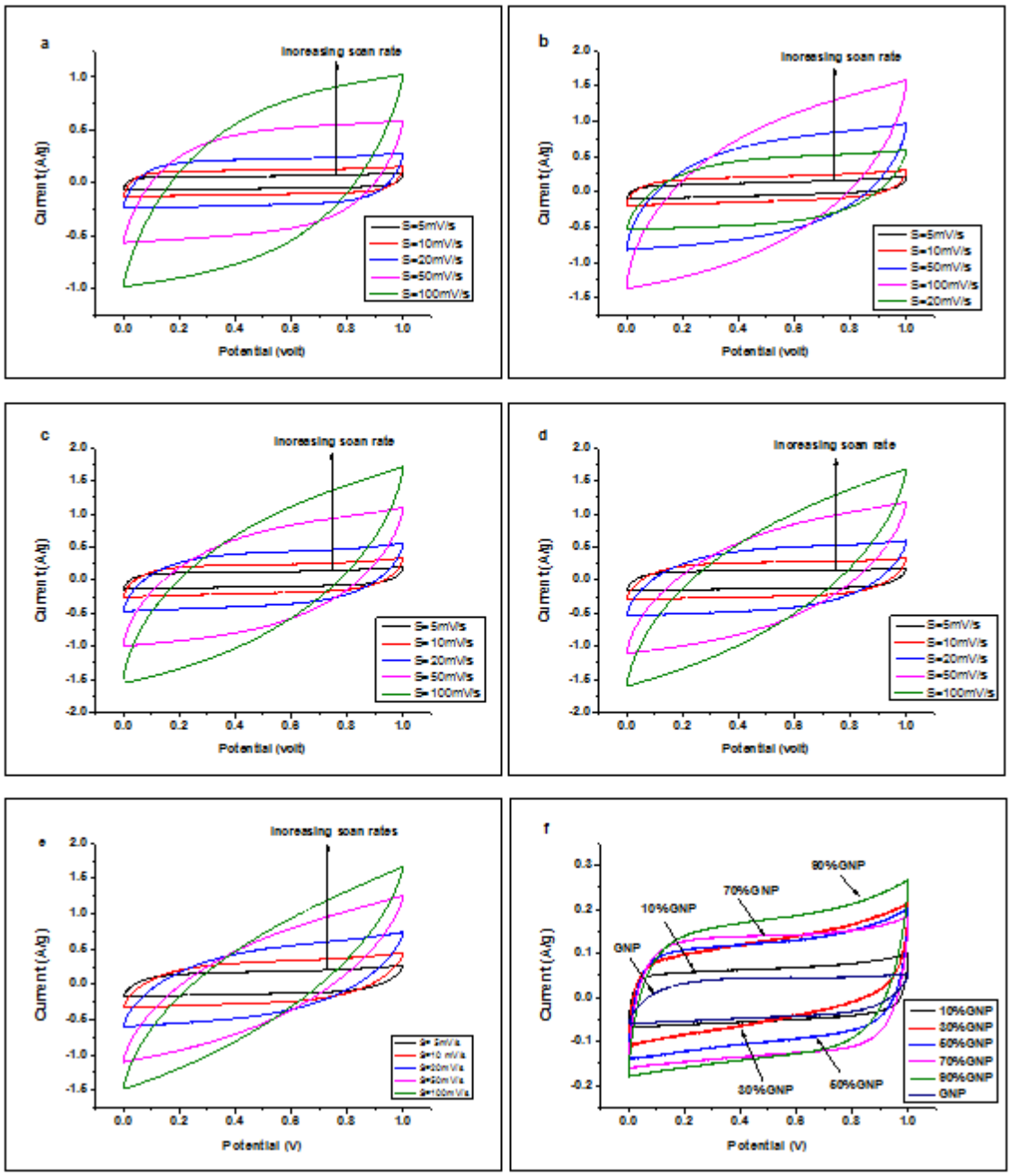

Fig. 4.1: CV curves at different scan rates (5, 10, 20, 50 and 100 mV/s) for CNF/ GNP composite with GNP weight percent of (**a**) 10%, (**b**) 30%, (**c**) 50%, (**d**) 70%, (**e**) 90% and (**f**) CV at scan rate 5 mV/s for all samples.

As observed for all samples, C_S values were decreasing with increasing scan rates. At low scan rate, ions have enough time to utilized all electrode vacant sites and diffuse through it. This indeed increase the electrode active area and hence the C_S will be higher. However, at higher scan rates, the

ions face difficulty to enter all vacant sites of the electrode. Hence, poorer rectangular shape and less C_S is obtained [83]. The high concentration near the surface restricted the diffusion into the pores, because not all ions had enough time to penetrate the inner pores and participated in charging process [81, 84].

Table (4.1): C_s (F/g) from CV for CNF/ GNP composite with different weight concentration of GNPs at different scan rates

Specific capacitance C_S (F/g)					
Scan rate (mV/s)	**10% GNP**	**30% GNP**	**50% GNP**	**70% GNP**	**90% GNP**
5	47.0	74.8	89.1	102.2	119.7
10	43.6	67.5	82.4	94.2	105.8
20	40.3	60.4	71.8	80.8	85.2
50	33.7	47.4	53.0	54.9	52.4
100	25.6	34.6	35.4	35.5	33.0

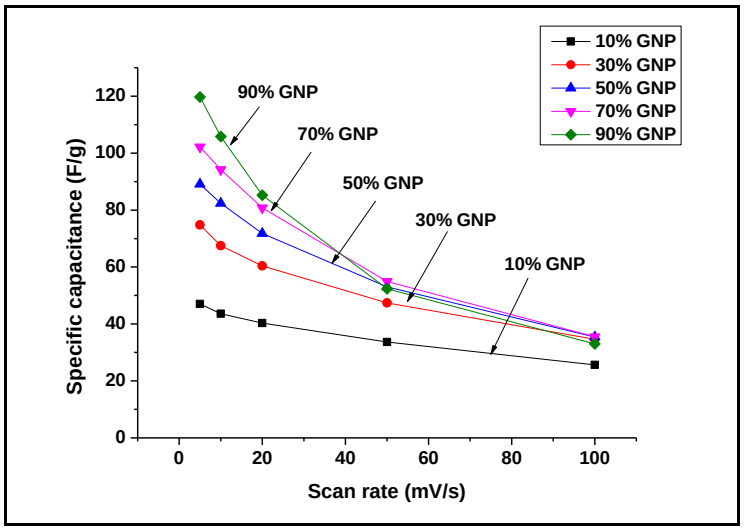

Fig. 4.2: Comparison of C_S at different scan rates for different concentration of GNPs.

For different concentrations of GNPs, C_S was found to increase with increasing GNP in the composite electrode (Figure 4.3). The highest C_S value achieved (for 90% of GNP) was 119.7 and 105.8 F/g at low scan rates of 5 and 10 mV/s, respectively. On the other hand, at high scan rates (50 and 100 mV/s), C_S increased with GNP contents up to 70% and then decreases at 90% of GNP. This is explained (as will be shown later in this thesis) by SSA, PSD and ion sieving; depending on ion absorption on their size in the electrolyte [19, 55, 82].

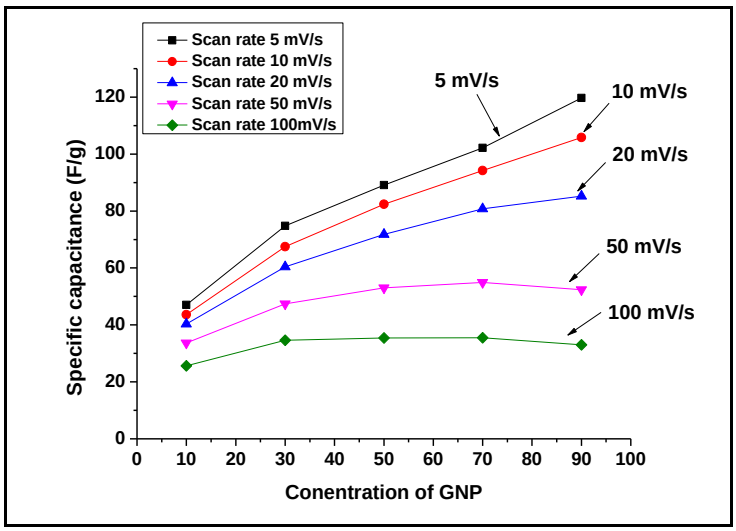

Fig. 4.3: Specific capacitance and GNP concentration at different scan rates.

Figure 4.4 shows CV stability of the samples. The C_S values were retained with 95% in the same range for the samples after 100 cycle at 100 mV/s. This indicates high stability, reversibility process and cycling life.

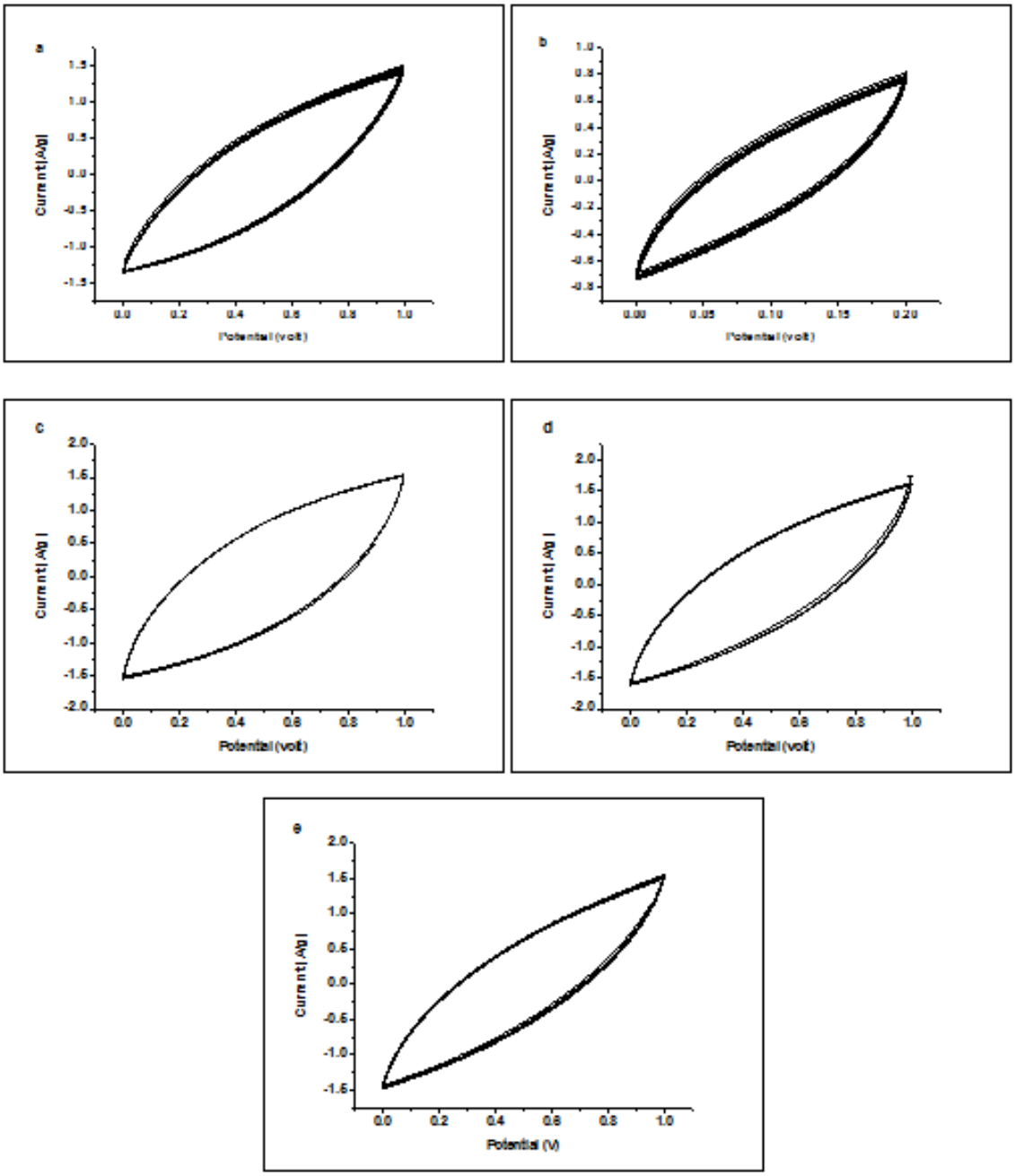

Fig. 4.4: Stability of CV at scan rate 100 mV/s for 100 cycle for CNF/ GNP composites with GNP weight percent of **(a)** 10%, **(b)** 30%, **(c)** 50%, **(d)** 70% and **(e)** 90%.

4.1.2: Galvanostatic charge/ discharge (GCD) behavior

The supercapacitive performance was also examined for CNF/ GNP composite at different concentration of GNPs by GCD method. Charge/

discharge for the SC electrodes was carried out in the range of (0- 1 volt) at different constant currents of 30, 50, 80 and 100 mA. At constant current, the capacitance of SCs depends on the electric field caused by variation of the potential by time [6- 9]. GCD curves for the samples are shown in figure 4.5. From GCD method, charging/ discharging processes and drop in potential can be measured exactly. Triangular shapes were appeared in GCD curves, due to the symmetrical linear charge/ discharge regions, which indicates high reversibility because of high ions response to the variation of potential [25, 66].

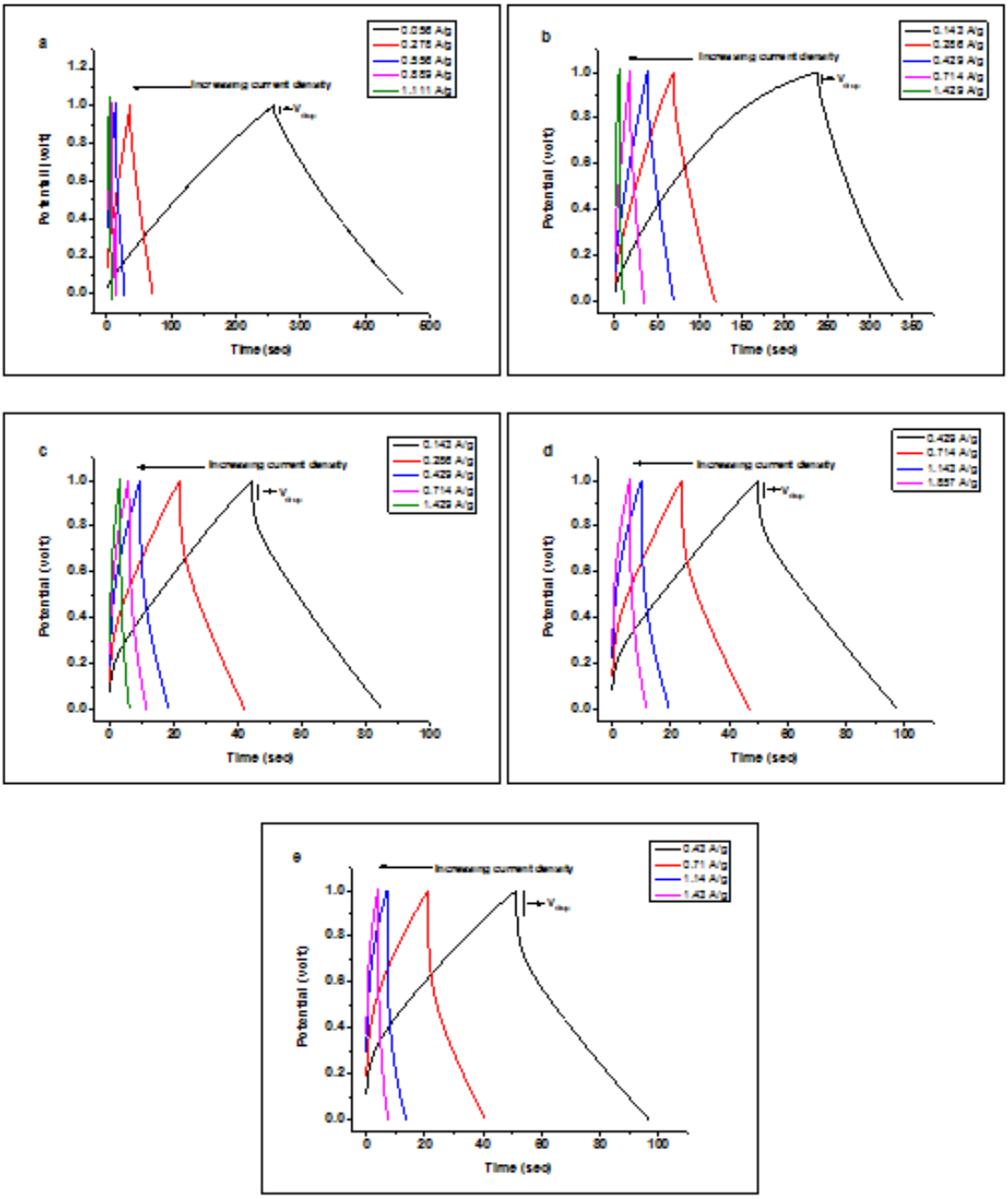

Fig. 4.5: GCDs for CNF/ GNP composites at different constant specific currents with GNP percentage weight of **(a)** 10%, **(b)** 30%, **(c)** 50%, **(d)** 70% and **(e)** 90%.

As shown in figure 4.5, the slope of the curve (dV/dt) was found to increase with increasing specific current. This is expected because with increasing currents the time which is needed for charge and discharge processes decreases, which is due to the high mobility of the ions [3, 66].

Due to this, decreasing in C_S values is expected as charge/ discharge current increased. This is consistent to C_S values that was observed in CV measurements and was found to decrease with increasing scan rate (dV/dt) [1, 18, 23, 25].

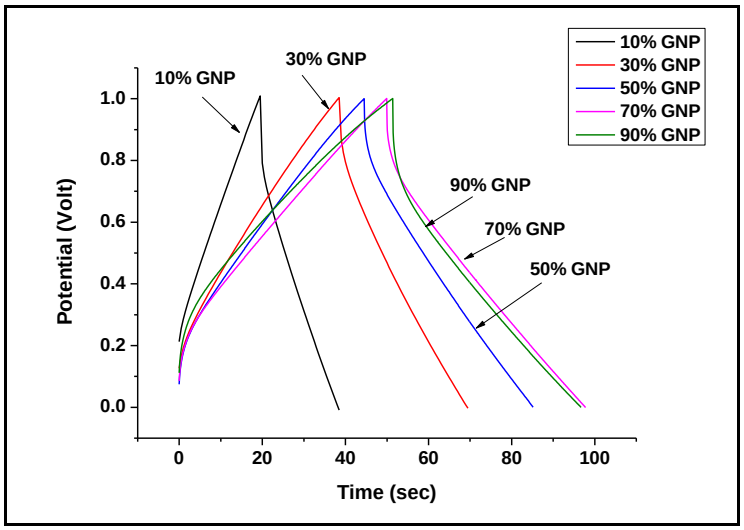

Fig. 4.6: GCD comparison at specific current (0.42 A/g) of different concentration of GNPs.

Figure 4.6 shows C_S comparison at specific current 0.42 A/g for all prepared samples. GCD areas increase with increasing GNP concentrations (dV/dt slope decreases), so C_S values increase. The C_S values for the samples were evaluated from equation (2.10) and are shown in table 4.2 at different current densities. C_S values increase from 21.62 to 54.6 F/g as GNP concentration increases from 10% to 90% at (0.42 A/g) specific current. This is because of increasing discharge time from 18.69 to 44.98 sec. So, longer charge/ discharge process means slower process and more ions can participate in process which causes high C_S value [66].

Table (4.2): C_S (F/g) from GCD for CNF/ GNP composite with different concentration of GNPs at different specific currents

Specific capacitance C_S (F/g)					
Specific current (A/g)	**10% GNP**	**30% GNP**	**50% GNP**	**70% GNP**	**90% GNP**
0.43	21.6	32.6	42.2	51.3	54.6
0.71	18.5	30.7	39.7	46.6	52.5
1.14	17.0	25.1	31.9	35.5	39.0
1.43	13.0	23.1	25.8	27.4	35.5

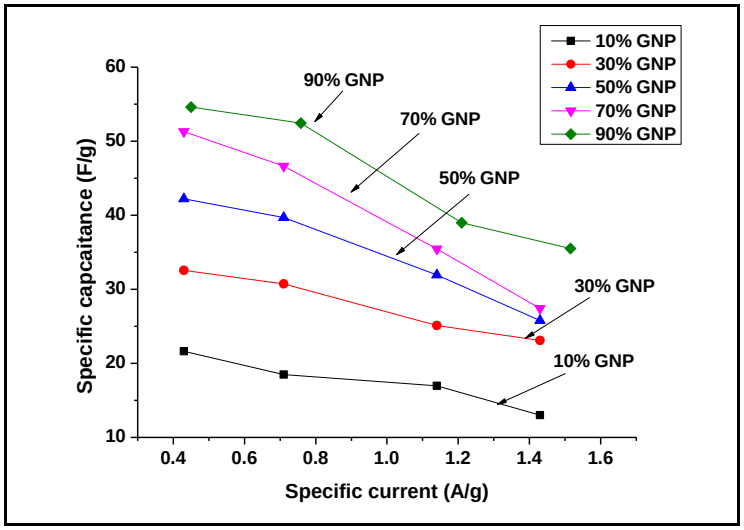

Fig. 4.7: C_S for CNF/ GNP composites at different specific currents and different concentration of GNPs.

The drop in potential (V_{drop}) after charging process and before discharging process was due to the loss of the potential in ESR [1, 3, 16]. Figure 4.8 shows the relation between the drop in potential with current. At all discharging current values V_{drop} decreases with increasing GNP weight of concentration up to 70%, then it increases for 90%. The smallest observed V_{drop} for 70% of GNP is due to the limited diffusion of the ions in the electrode/ electrolyte interface which depends on the type of pores and their volumes [18, 66]. For a good performance, it is essential to obtain the

smallest V_{drop} which indicates the highest conductivity with the smallest ESR and hence the highest power density [6- 8].

It is also observed that, in figure 4.8 the V_{drop} increases with increasing current. This behavior is normal if Ohm's law (V= I R) is considered. The lowest V_{drop} observed for sample of 70% GNP with V_{drop} ranges from 0.06 to 0.23 volt when current value changes from 30 to 100 mA. For the same current range, the highest V_{drop} from 0.12 to 0.55 volt was for the sample of 10% GNP.

ESR can be calculated in this method from the linear relation of V_{drop} and discharge current (V_{drop} = I R_{drop}) [16, 17, 19]. The calculated R_{drop} (ESR) was 5.57, 4.15, 2.32, 2.14 and 3.68 Ω for CNF/ GNP composite with 10%, 30% GNP, 50% GNP, 70% GNP and 90% GNP, respectively. So, the sample of 70% GNP has the lowest ESR (see figure 4.8). This points that the highest power density is for CNF/ GNP composite with GNP content of 70%.

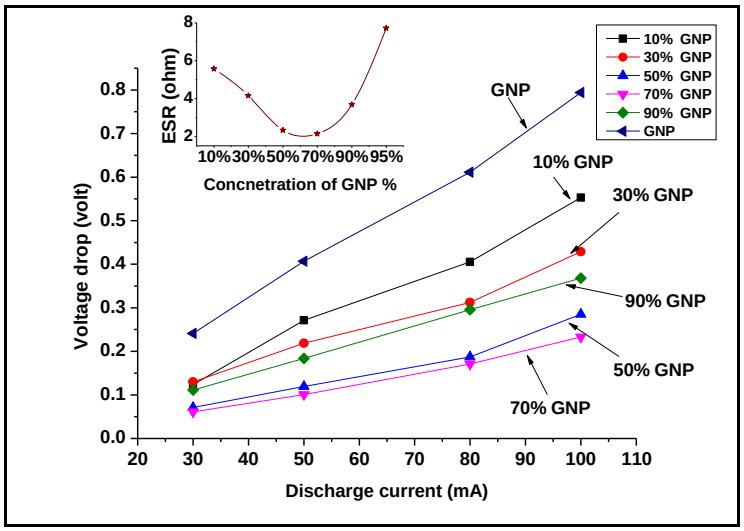

Fig. 4.8: Variation of voltage drop with discharge currents for different concentration of GNPs and shows the variation of ESR with percent content of GNP.

The charge/ discharge cycling stability up to 1500 cycles was tested for the samples at constant specific current 1.43 A/g. The values of C_S almost constant from first cycle to the last one as shown in figure 4.9. This stability indicates that the composite is perfect to be used as SC with long life cycle.

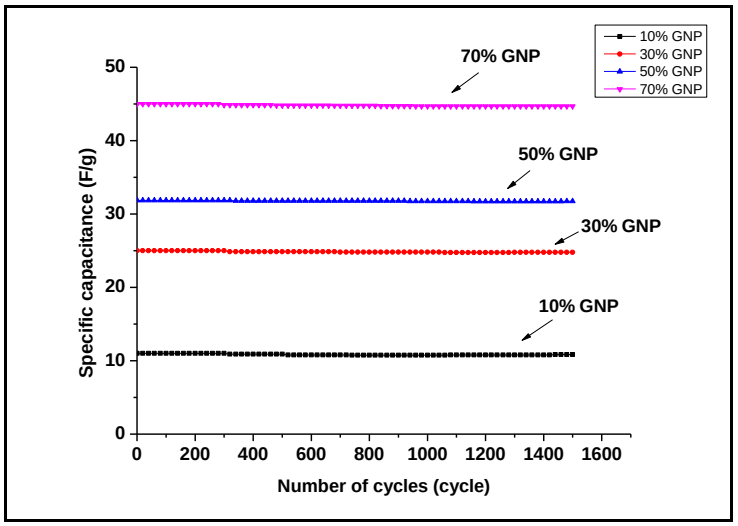

Fig. 4.9: Charge/ discharge cycling stability at constant specific current (1.43 A/g) for 1500 cycle for CNF/ GNP composites with different concentration of GNPs.

Power and energy densities can be evaluated by using equations (2.11) and (2.12) to construct Ragone plot (figure 4.10). We observed that both power and energy densities increase with increasing GNP weight concentration up to 70%, then they decrease for 90% concentration as shown in table 4. 3 and figure 4.10.

Power density depends on discharge current and discharge voltage difference (V) excluding V_{drop} as shown in figure 2.3 [23]. At highest current, the sample which had the highest voltage (V) can achieve the highest power density. As expected for all samples the power density is observed to increase with increasing discharge current (see table 4.3 and figure 4.10). The highest power density was 1095.4 W/kg observed for sample of 70% GNP measured at 100 mA discharge current.

Contrary to power density, maximum energy density can be obtained from the lowest discharge current (the highest discharge time) [18, 23]. As shown in table 4.3 and figure 4.10, the energy density is noticed to decrease with increasing discharge current. The maximum energy density was 5.26 Wh/kg observed for sample of 70% GNP measured at 30 mA.

This result of maximum power and energy densities, for sample of 70% GNP, indicates that this concentration is the optimized concentration of all CNF/ GNP composites used in this study.

Table (4.3): Power density and energy density for CNF/ GNP composites for different GNP weight concentration measured at different discharging current

% weight of GNP	Power Density (W/kg)				Energy Density (Wh/kg)			
	30 mA	50 mA	80 mA	100 mA	30 mA	50 mA	80 mA	100 mA
10%	243.4	351.6	404.9	528.3	2.32	1.79	1.51	0.87
30%	372.9	558.2	718.0	816.0	3.17	2.49	1.45	1.04
50%	396.0	617.1	890.3	1021.4	4.50	3.54	2.33	1.66
70%	398.9	629.1	928.6	1095.4	5.26	3.93	2.36	1.56
90%	404.0	618.2	853.8	957.0	5.05	3.35	1.57	0.88

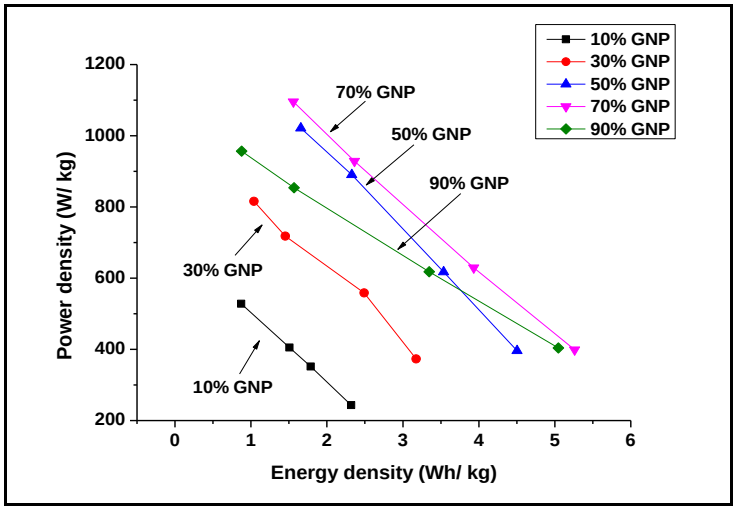

Fig. 4.10: Ragone plot of power density against energy density for different concentration of GNPs at different discharging current.

The efficiency (η) of the prepared SCs is evaluated by equation (2.14). All samples have a very good efficiency with small loss in energy (η= 0.88, 0.98, 0.92, 0.83 and 0.95) for samples of 90% GNP, 70% GNP, 50% GNP, 30% GNP and 10% GNP, respectively.

Hence, by GCD method, 70% GNP sample gave the highest energy density, the highest power density, the highest efficiency and the lowest ESR with high C_S value.

4.1.3: Electrochemical impedance behavior

EIS was performed to investigate the electrochemical behavior of the prepared CNF/ GNP composite electrodes. ESR and C_S were measured by applying small sinusoidal potential in the frequency range of 10 mHz to 100 KHz [17]. The measured signal was sinusoidal AC with amplitude 20 mV.

Figure 4.11 shows Nyquist plot for the all samples. The values of C_S in EIS method were calculated by using equation (2.18). The value of ESR is deduced from semi- circle of the Nyquist plot. Table 4.4 shows the values of C_S, R_S, R_{CT} and ESR of the samples.

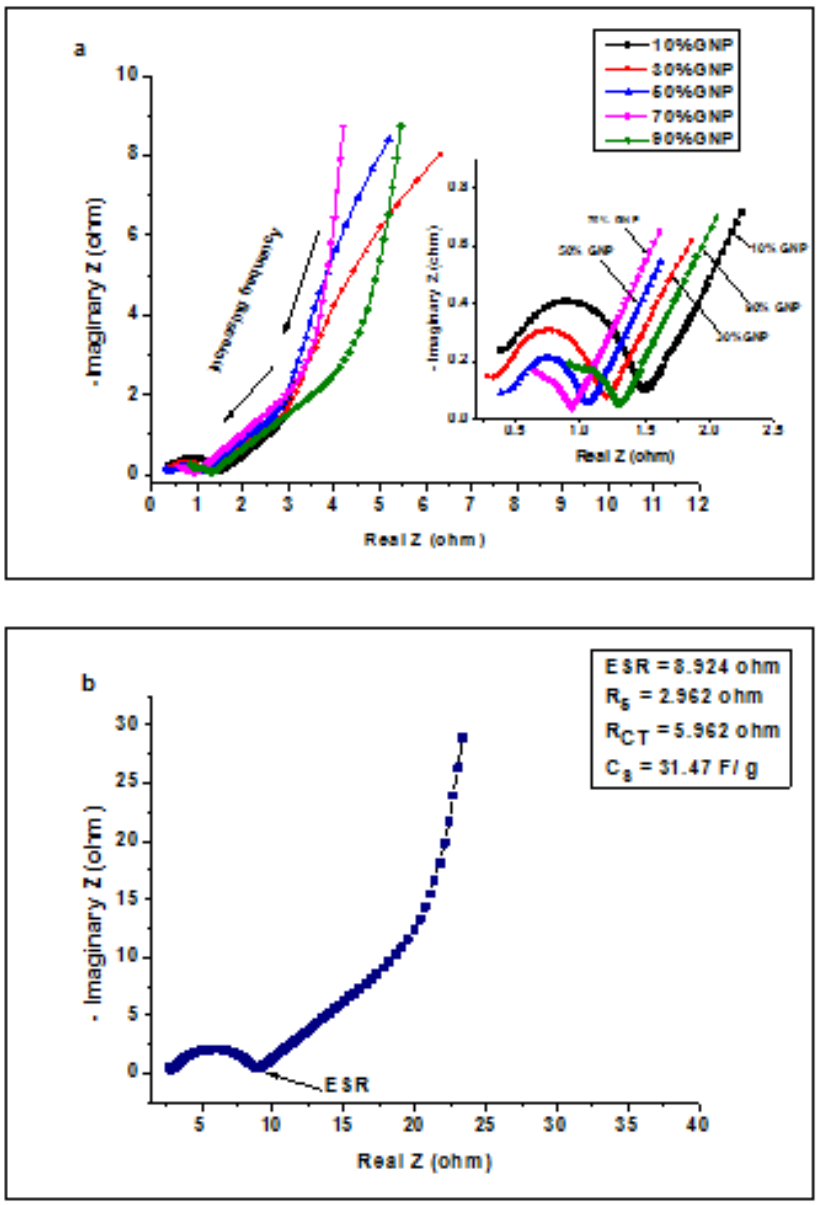

Fig. 4.11: (**a**) Nyquist plot for CNF/ GNP composite with different concentration of GNPs and (**b**) Nyquist plot for GNP sample

As shown in figure 4.11, the size of semi- circle became smaller with increasing concentration of GNPs up to 70%, then became larger for 90%. Smaller semi- circle in the high- frequency region indicates smaller ESR value [17, 66]. Also, the straight line in Warburg region has different deviations by changing GNP concentrations due to more diffusion because

the ions move farther towards the pores. The deviation of the vertical line in the low- frequency region from the straight line in the mid- frequency region becomes less with increasing GNP weight up to 70% of GNP sample, then more deviation in the vertical line for 90% of GNP sample. Less deviation was related to nearly ideal capacitive response [6, 66, 70, 71].

Table 4.4 shows the measured resistances. ESR values decreases with increasing concentration of GNPs until it reaches 0.632 Ω for 70% of GNP, then ESR increases to 1.26 Ω for 90% of GNP sample. The lowest ESR values indicate easy penetration and diffusion into the electrode surface [3, 17]. So, the conductivity of the prepared SC increased [3]. Therefore, sample of 70% GNP had the highest conductivity so highest power density is observed as mentioned in the previous section.

Table (4.4): Resistances and C_S comparison for CNF/ GNP composite with different weight concentration of GNP by EIS method

Parameters	10% GNP	30% GNP	50% GNP	70% GNP	90% GNP
C_S (F/g)	50.9	66.3	91.4	104.2	123.1
R_S (Ω)	0.398	0.346	0.372	0.317	0.911
R_{CT} (Ω)	1.082	0.625	0.336	0.315	0.379
ESR (Ω)	1.480	0.971	0.708	0.632	1.260

The electrolyte resistance (R_S) had small values for all samples. Samples of 10% GNP and 50% GNP had the same range value of R_S which is about 0.4 Ω. For 30% GNP and 70% GNP had the smallest value of R_S which is about 0.35, 0.32 Ω, respectively. This indicates that 1M KOH aqueous electrolyte had high ionic conductivity [18]. So, the ions of the electrolyte

didn’t have constrains on movement and diffusion towards the pores into the electrode surface. However, sample of 90% GNP had the highest value of R_S (0.911 Ω). This is due to its structure which limit the ions diffusion through it.

Charge transfer resistance (R_{CT}) values decrease with increasing GNP concentrations. R_{CT} represents the charge transition between electrode and electrolyte, which depends on the diffusion towards or away the electrode surface [70, 71]. So, by increasing GNP concentrations, the ions can go deeply into the pores of the electrode surface to form the electrode/ electrolyte interface according to the pore volumes which were participating into the charging process [18]. The lowest R_{CT} (0.315 Ω) was also for the sample with 70% GNP.

The specific capacitance values for the prepared SCs depends on the frequency and the imaginary part of the impedance (equation 2.18) [6- 8]. The relation between C_S and frequency was shown in figure 4.12 (a). As the frequency increases, C_S values decrease. The highest value of C_S was obtained for all samples at the lowest frequency value (0.01 Hz). This is due to the inversely proportional relation between the permittivity of the electrolyte and signal frequency [85, 86]; the permittivity was increased by decreasing frequency, so the electric field was also decreased. So the concentration of the ions also became less near the surface of the electrodes. But, because all the ions had enough time to penetrate and went deeply into the pores. C_S values were increased [18, 85, 86]. Moreover, the

number of the ions which participated in charging SC were increased with increasing GNP concentration. Therefore, C_S value was also increased, and hence higher energy density can be stored. The best capacitive performance was for 90% of GNP sample, the highest value of C_S is 123.1 F/g observed at 0.01 Hz.

The time constant (τ) for the samples can then be calculated from equation (2.19). It was 6.78, 4.56, 4.53, 4.6 and 10.24 s for 10% GNP, 30% GNP, 50% GNP, 70% GNP and 90% GNP, respectively. All samples had a good capacitive response. 30% GNP, 50% GNP and 70% GNP had the smallest time constant so they had the smallest time needed for charge/ discharge process.

Sinusoidal current was resulted with phase shift due to the applied sinusoidal potential at the same frequency. Phase angle determined mathematically by determining the real and the imaginary parts of impedance ($\varphi = \arg(Z)$) [70, 71]. Figure 4.12 (b) shows the variation of phase angle with frequency (Bode plot). As the frequency decreased, the phase angle increased. For resistor behavior at high frequency, the phase angle must approach zero ($Z = R$) [17, 70].

The phase angle was found to decrease with increasing GNP concentrations up to 50%, then increased for 70% and 90%. At 100 KHz, the phase angle was ($-38.79^{\circ}, -3.2^{\circ}, -3.47^{\circ}, -11.53^{\circ}$ and -11.05°) for 10% GNP, 30% GNP, 50% GNP, 70% GNP and 90% GNP, respectively. The highest phase angle was obtained at the lowest frequency value. As the phase angle

approach (-90°) the capacitive behavior becomes dominant as for ideal capacitor the impedance is $Z = \frac{1}{j\,\omega\,C}$ [17, 18]. At 0.01 Hz, the capacitive behavior for 10% GNP and 90% GNP were in the same range (-56.45° and -54.74°), respectively. And the best capacitive performance was for 30% GNP, 50% GNP and 70% GNP samples, the phase angle for them approached $-65.85^{\circ}, -66.47^{\circ}$ and -64.33°, respectively.

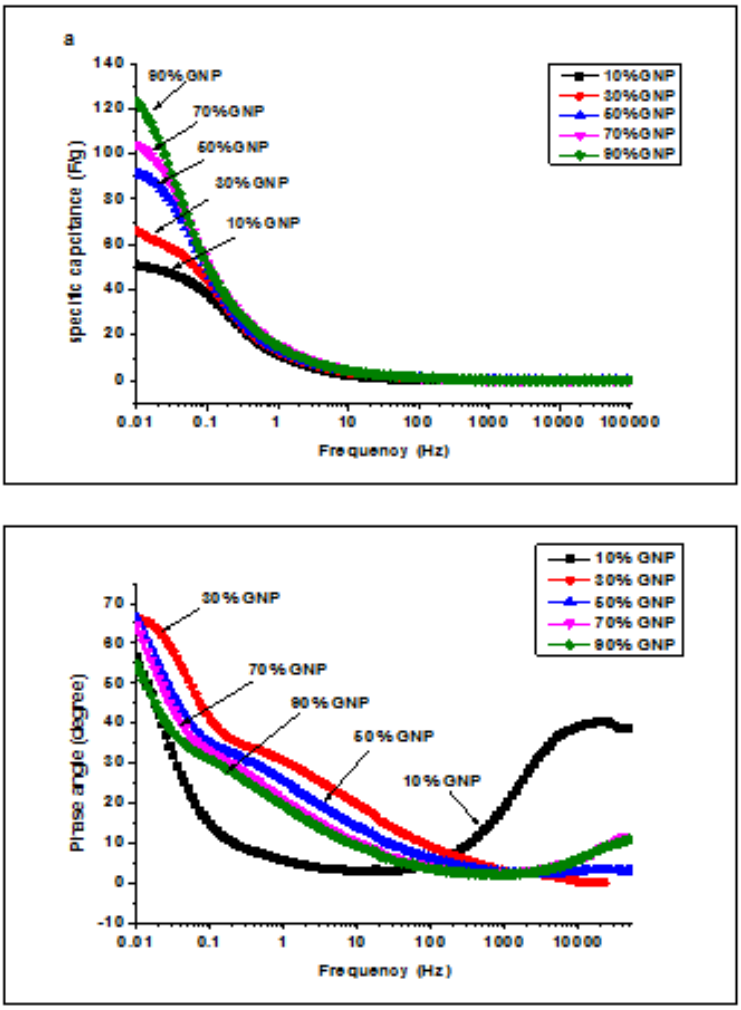

Fig. 4.12: comparison for all samples by EIS (**a)** specific capacitance and **(b)** phase angle as a function of logarithm of frequency.

Figure 4.13 (a) shows the real part of impedance as a function of logarithm of frequency. Electrolyte and charge transfer resistances can be obtained from this plot. The lowest value of ESR was at the highest frequency value (100 KHz) which represented the electrolyte resistance which was about 0.3 Ω for 10% GNP, 30% GNP and 50% GNP samples, then ESR value increased to about 0.7 Ω for 70% GNP and 90% GNP samples. When the value of the frequency achieved (316.46 Hz) sharp increase in the real part of the resistance for 10% GNP sample relative to the others. This is due to its dominant CNF structure. At 0.01 Hz resistance reached 9.2, 6.32, 4.5, 4.2 and 5.52 Ω for 10% GNP, 30% GNP, 50% GNP, 70% GNP and 90% GNP, respectively. Decreasing the value of the frequency means increasing the time which is needed for ions to penetrate the pores. So, the number of the ions which participate into charge/ discharge processes increases which leads to fill some type of pores easier, but some of them needs more time for ions to go deeper into them, hence, the ions move longer displacement and diffusion layer increases within the electrolyte. This causes low conductivity and high ESR [18, 39, 85]. For 70% GNP sample the ions that penetrate into the pores more than the other samples so its resistance was the lowest (this will be explained later in the next section of this chapter).

Figure 4.13 (b) shows the inverse relation between the imaginary part of the impedance and frequency. At high frequency, the imaginary part of the impedance decreases until it reaches zero (resistor behavior) [70, 71]. As expected, the behavior of samples follows ideal capacitor behavior; when the frequency value decreases the imaginary part of the impedance

increases until it reaches $Z = 1/(j\omega C)$ [17]. At 100 KHz, the imaginary part is $(-0.74, -0.18, -0.41, -0.59 \text{ and } -0.55\ \Omega)$, then at 10 mHz it reaches $(-13.89, -13.72, -9.95, -8.73 \text{ and } -7.8\ \Omega)$ for 10% GNP, 30% GNP, 50% GNP, 70% GNP and 90% GNP, respectively. The transition between resistor and capacitor behaviors can be explained by determining knee frequency (f_0) which is at 45°. At this angle, one can evaluate the relaxation time (τ_0) which is important for determination of capacitor performance [6- 8]. For the frequency values which are larger than the knee frequency, SC behaves as pure resistor, and for the values of frequency smaller than the knee frequency, SC behaves as pure capacitor. If SC transition from resistor to capacitor behavior occurred at high frequency, it means that the SC had small relaxation time and had a good capacitor performance [18]. Relaxation time was 4.24, 1.48, 0.886, 1.028 and 0.811 s for 10% GNP, 30% GNP, 50% GNP, 70% GNP and 90% GNP, respectively. All samples show relatively small relaxation time so they can transfer from resistor to capacitor behavior much faster and hence they have good capacitive performance.

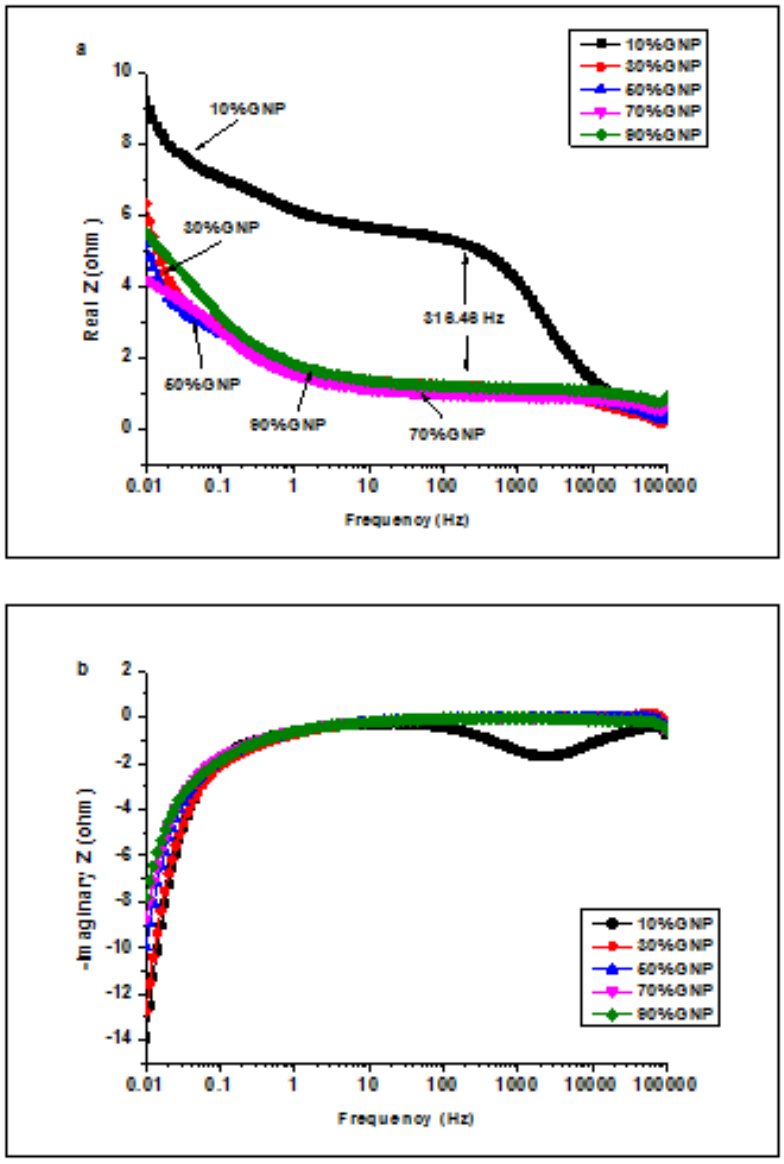

Fig. 4.13: (**a)** Real and (**b**) imaginary parts against log of frequency, respectively for all samples.

As discussed in this section, 70% of GNP sample had the smallest ESR, small τ, fast ion response and optimized high value of C_S. Which indicates a very good capacitive behavior. So, it can achieve a very high power density due to its small ESR. And it can store high energy density due to its high specific capacitance value. These results from EIS method were complementary to CV and GCD results.

The object of enhancing the performance of SC was achieving high power density, high energy density, small ESR, small time constant, fast transition to capacitor behavior while keeping C_S value as high as possible. These properties had best values and optimized for CNF/ GNP composite with 70% weight concentration of GNP. This composite have high power density of $1095.43\ W/kg$, high energy density of $5.26\ Wh/kg$, high specific capacitance of $102.2\ F/g$, small ESR of $0.632\ \Omega$ and high efficiency of 98%.

These results of CNF/ GNP composite with 70% weight concentration of GNP enhanced the specific capacitance value of the SC which is based on CNF electrodes and the ones which is based on GNP. The specific capacitance value of CNF electrodes reached $52\ F/g$at scan rate $5\ mV/s$ [18]. For GNP electrodes in 1M KOH achieved $32.5\ F/g$ at scan rate $5\ mV/s$ (figure 4.1 (f)). As expected, CNF/ GNP composite store more energy density relative to SC based on CNF electrodes alone and GNP electrodes alone, which have limited energy density, that is around $2.3\ Wh/kg$ for CNF [18], and $3.6\ Wh/kg$ for GNPs. However, CNF has small ESR (about $0.2\ \Omega$) due to its high conductivity, hence, it can reach a very high power density ($1860\ W/kg$) [18]. On the other hand, GNPs have very high value of ESR, which is around $9\ \Omega$ (figure 4.11 (b)) measured by EIS method. This reason of small power density of GNP sample which reaches the maximum value of $444.6\ W/kg$. So, adding CNFs to GNPs decreases ESR value of GNP which causes an increase in the value of power density.

4.2: Structural, morphological behavior and pore texture

The SSA, pore volume and PSD of CNF/ GNP composite with different concentrations of GNP which were used as SC electrodes were investigated by different techniques. The achieved electrochemical results can be explained based on SSA and PSD. The following sections show the results and discussion of the samples which were used in this thesis.

4.2.1: Structural and morphological behavior

The surface morphology and structure of the prepared electrodes were examined by SEM (Jeol J- 7100) and TEM (Jeol 2011). Figures 4.14 and 4.15 show SEM and TEM results for all samples.

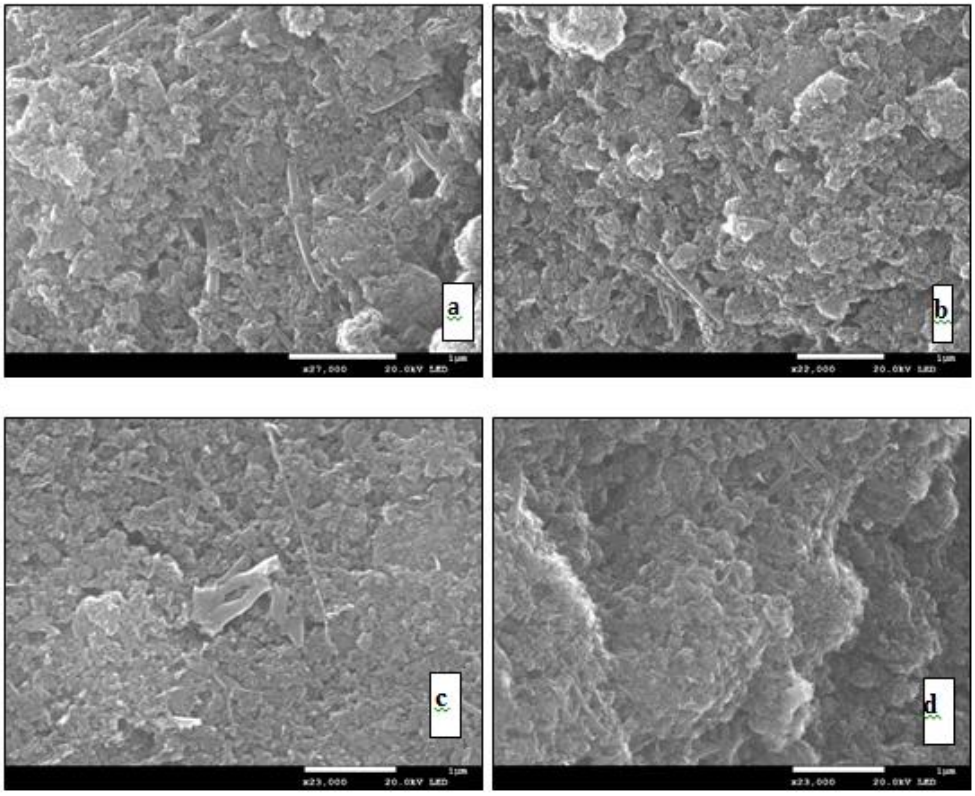

Fig. 4.14: SEM images for CNF/ GNP composites with different concentration of GNP **(a**) 10% GNP, (**b)** 30% GNP, (**c)** 50% GNP and **(d)** 70% GNP.

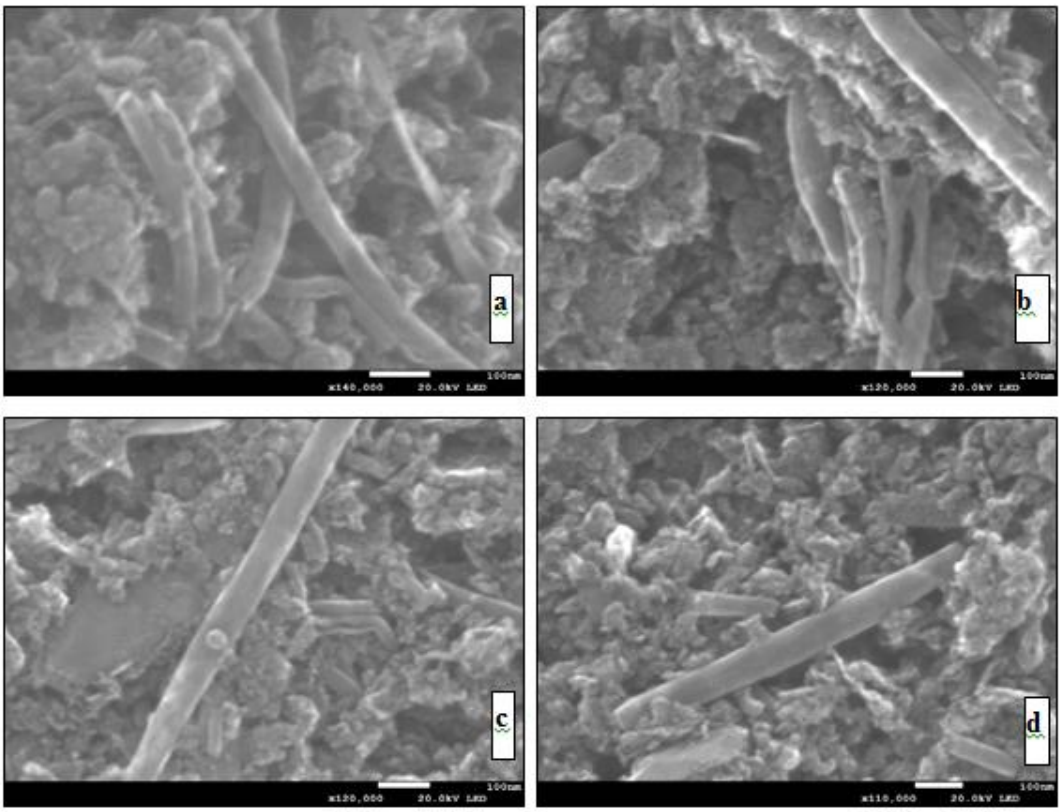

Fig. 4.15: TEM images for CNF/ GNP composites with different concentration of GNPs **(a)** 10% GNP, (**b)** 30% GNP, (**c)** 50% GNP and (**d)** 70% GNP.

SEM shows the external structure for CNF/ GNP composites with different concentration of GNP (figure 4.14). The intrinsic structure for the samples were examined by taking cross- section of the samples with high resolution, TEM (figure 4. 15). As shown in figures 4.14 and 4.15, CNF structure had cylindrical shape, and GNP had planer structure like sheet texture. The cylindrical CNFs arranged between the layers of GNPs. As shown in SEM and TEM images, as GNP concentration increases the structure of CNF/ GNP composite trends from cylindrical fiber shape dominant to sheet shape dominant. Due to this SSA increased as expected.

CNF/ GNP composites contain different pore sizes which decrease with increasing GNP concentration as observed from TEM images (figure 4. 15). The material becomes denser, because of this the ions of the electrolyte can move easier through the pores of the material, as will discussed later in the next section of this chapter [19, 86].

4.2.2: Pore texture of electrode materials

The SSA and PSD of CNF/ GNP composite for the prepared electrodes were obtained by using N_2 adsorption/ desorption isotherms by using BET analyzer (TriStar 3000 V6. 04A). SSA of the electrodes was calculated by BET method, while PSD was determined by BJH desorption, MP and Harkins- Jura methods.

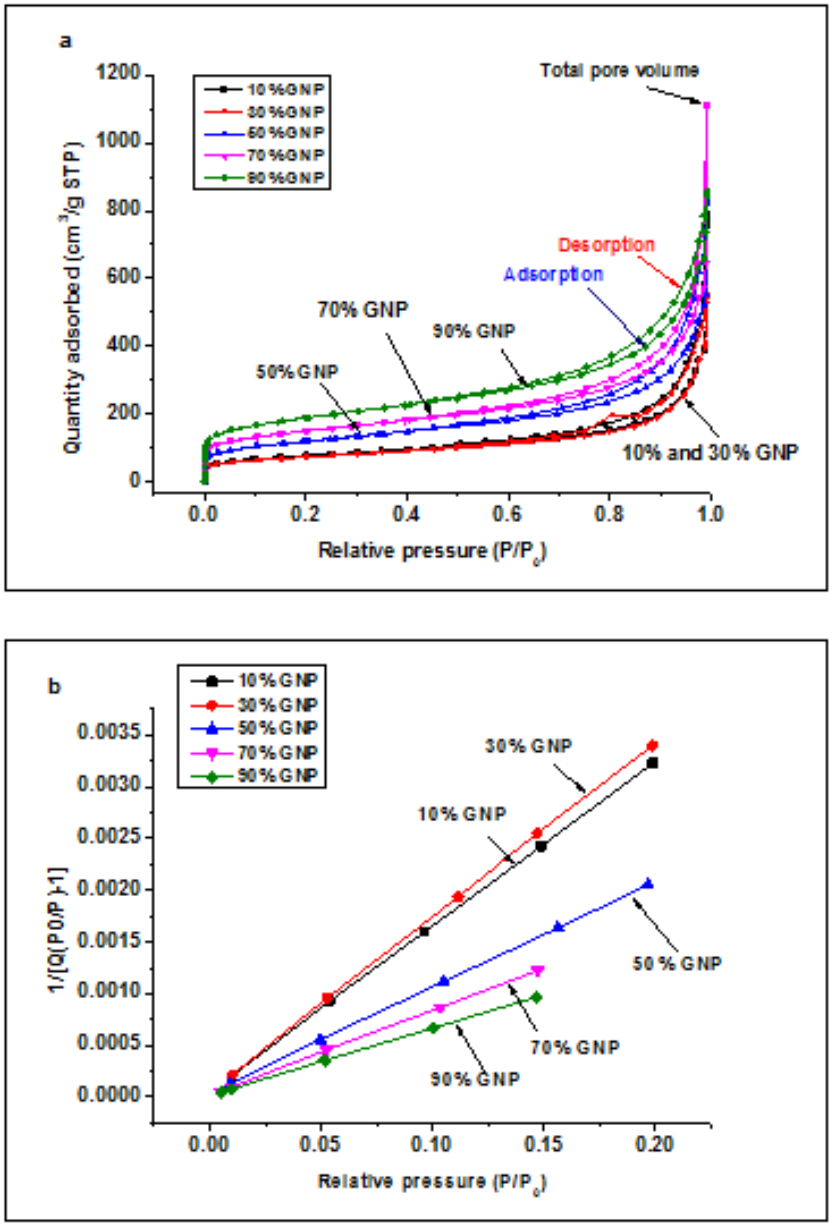

Fig. 4.16: **(a)** Nitrogen isotherms and **(b)** SSA from BET plot for CNF/ GNP composites with different concentration of GNPs.

Figure 4.16 (a) shows Nitrogen adsorption/ desorption isotherm for different concentration of GNPs. The quantity adsorbed (in $\frac{cm^3}{g}$ STP) denoted to the adsorbed volume. As shown in figure 4. 16 (a), the adsorbed quantity was increased as relative pressure on the sample. This is due to increase the force on nitrogen molecules. Nitrogen adsorption/ desorption

isotherm (figure 4.16 (a)) presented a small hysteresis loop in the middle range of relative pressure (0.4- 0.9). According to IUPAC, all samples were IV type [6- 8]. This indicates that mesopores with cylindrical shape are contained in the samples [6, 7]. The bending in the beginning of the curves near the origin indicate that micropores are also contained in the sample [73- 75].

Total pore volume (V_{tot}) is calculated from the quantity of adsorbed nitrogen measured at relative pressure unity ($\frac{P}{P_0} \approx 0.9924$) [72- 74]. V_{tot} was decreased as GNP concentration increased from 10% to 30%, then it increased as GNP concentration increased up to 70% GNP sample, then decreased again for 90% GNP sample (see table 4.5). For converting the quantity adsorbed from gas state (in $\frac{cm^3}{g}$ STP) to liquid state (in $\frac{cm^3}{g}$), one must multiply the quantity adsorbed by 0.001547 according to:

$$V = \frac{m}{\rho_l} = \frac{n\,M}{\rho_l} = \frac{V_{ads}}{V_{STP}}\,(V_l) = \left(\frac{V_l}{V_{STP}}\right) V_{ads} \qquad (4.1)$$

$$\text{Or} \quad V = \frac{m}{\rho_l} = \frac{\rho_{STP}\,V_{ads}}{\rho_l} \qquad (4.2)$$

Where V is the volume, ρ_l is liquid nitrogen density ($0.807\ g/mL$), n is the number of moles, M is the molecular weight, V_{ads} is the adsorbed volume, V_l is liquid nitrogen volume ($34.7\ cm^3/g$), V_{STP} is the standard gas volume ($22412\ cm^3/g$) and ρ_{STP} is the STP density of nitrogen ($1.2 * 10^{-3}\ g/mL$).

The values of the total pore volume are listed in table 4.5. Which was varied from 1.22 to 0.855 cm^3/g for GNP concentration from 10% to 30%, then increased up to 1.72 cm^3/g for 70% GNP sample, after that decreased for 90% GNP (1.33 cm^3/g). The arrangement of CNFs between the layers of GNPs caused a decrease in the volume could be attributed to closing the pores for 30% GNP and 90% GNP samples.

Table (4.5): Physicochemical parameters of the samples

Parameter	10% GNP	30% GNP	50% GNP	70% GNP	90% GNP
SSA (m^2/g)	271.27	257.76	423.29	528.52	665.93
$S_{ultra-micro}$ (m^2/g)	73.50	67.99	104.70	542.13	673.90
S_{micro} (m^2/g)	50.50	46.80	71.11	138.94	148.93
S_{meso} (m^2/g)	215.90	215.94	328.22	358.28	450.18
S_{macro} (m^2/g)	24.27	11.64	18.33	29.27	12.81
S_{ext} (m^2/g)	220.77	210.96	352.18	389.58	481.15
V_{tot} (cm^3/g)	1.22	0.86	1.29	1.72	1.33
$V_{ultra-micro}$ (cm^3/g)	0.0232	0.0215	0.0354	0.2341	0.2868
V_{micro} (cm^3/g)	0.0225	0.0208	0.0313	0.0614	0.0813
V_{meso} (cm^3/g)	0.5508	0.5371	0.7433	0.7581	0.8837
V_{macro} (cm^3/g)	0.6413	0.2865	0.4805	0.8798	0.3324
C_S (F/g)	47.0	74.8	89.1	102.2	119.7

S_{micro}, V_{micro} micro area and volume form t- plot (larger than 0.7 nm).

S_{ultra}, V_{ultra} ultra micro area and volume from MP method (smaller than 0.7 nm).

S_{meso}, S_{macro}, V_{meso}, V_{macro} meso and macro areas and volumes from BJH desorption method.

S_{ext} external area from t- plot.

C_S specific capacitance from CV at scan rate 5 mV/s.

SSA was extracted from the linear BET plot (figure 4.16 (b)) in the range of (0.002- 0.2) relative pressure. SSA was calculated according to equation (2.15) [73, 74]. For converting the monolayer quantity adsorbed from STP (in $\frac{cm^3}{g}$ STP) to ($\frac{cm^3}{g}$) by dividing it by $22414\ cm^3$. As listed in table (4.5), the increase in SSA was (59.26%) with increasing GNPs concentration except 30% GNP sample. 90% GNP sample had the largest SSA which is $665.93\ m^2/g$ and the smallest SSA is for 30% GNP sample which is $257.76\ m^2/g$. So, increasing SSA and total pore volume were due to adding GNPs which didn't block pores, unlike adding polymers which decrease porosity [49].

Meso and macro volumes and areas were investigated by BJH desorption in diameter range (17 to $3000\ A^0$). However, this method can't identify micropores because Kelvin equation isn't valid for narrow pores [6- 8, 11]. Incremental volumes were calculated according to the thickness of the adsorbed layer at each relative pressure [74]. Incremental meso volume evaluated in (18- 496.5 A^0) diameter range, and incremental macro volumes (623.8- 2532.7 A^0) diameter range. Cumulative meso volumes were increased from (0.5508 to $0.8837\ cm^3/g$) as GNP concentration increased from 10% to 90%. However cumulative macro volumes were decreased from (0.641 to $0.287\ cm^3/g$) when GNP concentration increased from 10% to 30%, then increased up to 70% of GNP concentration (up to $0.8798\ cm^3/g$). After that macro volume decreased for 90% GNP sample which reached $0.3324\ cm^3/g$. Also, cumulative meso areas were changed from 215.9 to $450.18\ m^2/g$ for increasing GNP

from 10% to 90% weight. Cumulative macro areas were changed similarly as cumulative macro volumes for the samples, the largest macro area was 29.27 m^2/g for 70% GNP sample as also listed in table 4.5.

Harkins and Jura method was used to determine micro volume and area [76]. Figure 4.17 shows t- plot, the relation between the quantity adsorbed and thickness in the range of (3.7 to 5 A^0). All samples didn't pass through the origin and the curves were bent near the origin which indicates that micropores existed in the materials [76- 79]. Y- intercept of the plot was denoted to micropore volume (V_{micro}) after multiplying the quantity adsorbed by (0.001547) for converting. Micropore volumes increased with increasing GNP concentration as listed in table 4.5. The values of micro volumes increased from 0.0225 to 0.0813 cm^3/g for 10% GNP to 90% GNP. At high pressure, the slope of the line is used to calculate the external area, the slope is multiplied by (15.47) to convert the area from ($\frac{cm^3}{g\ A^0}$ STP) to (m^2/g). As shown in table 4.5, small decrease from (220.77 to 210.96 m^2/g) in external area with increasing GNP from 10% to 30% was observed, then increased up to 481.15 m^2/g for 90% GNP sample. Micro areas were calculated by subtracting external area from SSA. Micro area was varied from 50.5 to 148.93 m^2/g with increasing GNP concentration from 10% to 90%.

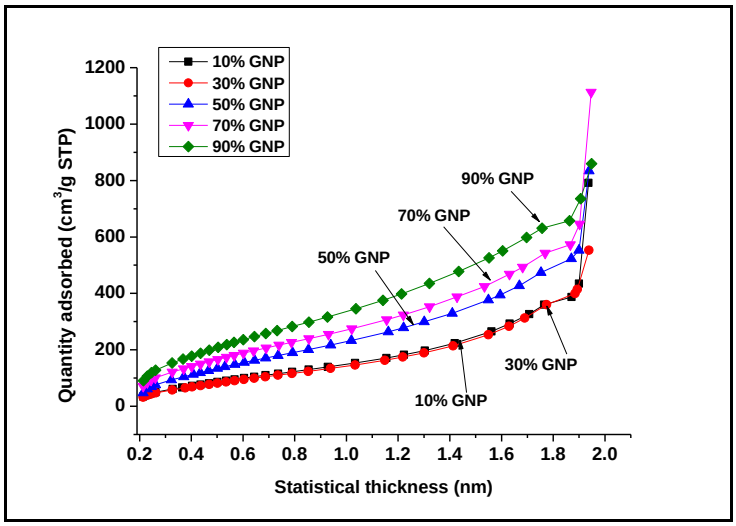

Fig. 4.17: t- plot for CNF/ GNP composite with different concentrations of GNP.

The micropores (smaller than 0.7 nm) which didn't detect in t- plot was distinguished by MP method which is an extension to the t- plot method in the range of (2.6 to 5 A^0) hydraulic radius [79]. These micro pores are called ultra- micropores. As illustrated in table 4.5, the first three samples had the same range of ultra- micro volume from 0.02 to 0.03 cm^3/g. Then, an observed increased in ultra- micro volume for 70% GNP and 90% GNP samples which was 0.234 and 0.2868 cm^3/g, respectively. Ultra-micro area had a small decrease by increasing GNP from 10% to 30% weight. After that it was increased up to 673.9 m^2/g for 90% GNP sample.

The SSA deviated from the sum of micro, meso and macro areas. This indicates presence of ink- bottle pores which was not detected [87]. SSA depends on the accuracy of the used method. BET method which was used for calculations gave very close value to the total area.

The distribution of the pores depends on the size of pores, and independent of the external area [88]. PSD was determined after calculating pore volumes and areas. The diameter of the pores was distinguished from BJH desorption, t- plot and MP methods [6- 8].

BJH desorption of $(\frac{dV}{d \log D})$ plot was used to determine PSD of mesopores and macropores. Figure 4.18 shows the dominate mesopores and macropores in the samples. The first three samples had the same range pore diameter in the range of $(3.4 - 3.87\ \text{nm})$. 70% GNP sample had three peaks in the plot: the first peak in the range of $(1.78 - 2.02\ \text{nm})$, the second peak in the range of $(3.52 - 3.92\ \text{nm})$ and the third peak in the range of $(143.01 - 197.45\ \text{nm})$. However, 90% GNP had two peaks: the first one in the range of $(27.7 - 44.54\ \text{nm})$ and the second one in the range of $(82.87 - 142.68\ \text{nm})$. All samples had dominate mesopores with small diameter $(< 4\ \text{nm})$. But, the sample of 90% GNP had mesopores larger than the other samples. On the other hand, 70% GNP sample had dominante macropores in addition to the mesopores.

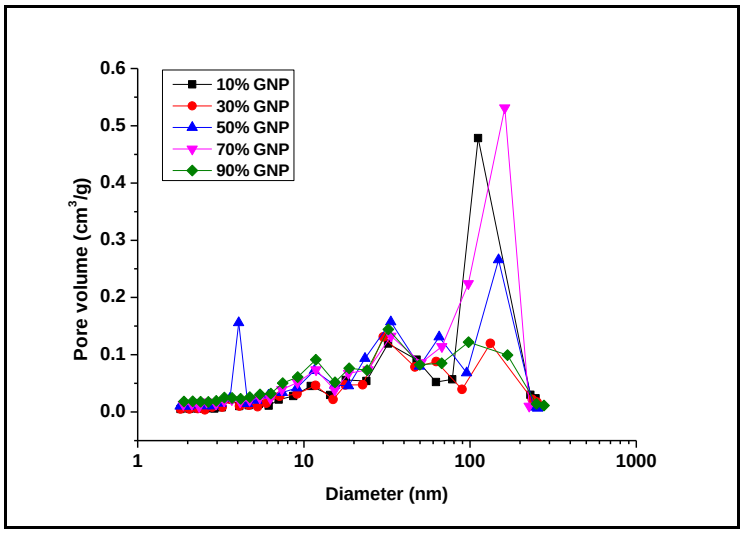

Fig. 4.18: PSD for CNF/ GNP composites with different concentration with GNPs by BJH desorption $\frac{dV}{d\log D}$.

The average BJH diameter ($\frac{4\,V_{BJH}}{S_{BJH}}$) decreases from (19.854 to 14.125 nm) when GNP concentration increases from 10% to 50%, then it increases to (16.9 nm) for 70% GNP sample. After that, it decreases again for 90% GNP sample (10.506 nm) as listed in table 4.6.

The average pore hydraulic radius ($\frac{V_{ultra}}{S_{ultra}}$) is calculated from MP method. It increases with increasing GNP concentration. The average pore hydraulic radius for 10%, 30% and 50% weight concentration of GNP is 0.3 nm, but it increased to 0.4 nm for 70% GNP and 90% GNP samples as listed in table 4.6.

Table (4.6): Pore size and pore volume percentage for CNF/ GNP composites with different GNP concentration

Sample	Diameter by BJH method (nm)	Hydraulic radius MP method (nm)	Average pore width (nm)	P_{micro} (%)	P_{ultra} (%)	P_{meso} (%)	P_{macro} (%)
10% GNP	19.8535	0.315	18.0579	1.84	1.89	44.97	52.37
30% GNP	14.475	0.3155	13.2736	2.44	2.51	62.8	33.5
50% GNP	14.1249	0.3385	12.1952	2.43	2.75	57.6	37.23
70% GNP	16.9062	0.4319	13.0345	3.56	13.59	44.02	51.09
90% GNP	10.5064	0.4256	7.988	6.11	21.56	66.44	24.99

$P_{micro} = V_{micro}/ V_{tot} *100\%$, $P_{ultra} = V_{ultra}/ V_{tot} *100\%$, $P_{meso}= V_{meso}/ V_{tot}*100\%$, $P_{macro}= V_{macro}/ V_{tot} *100\%$

BJH diameter= 4 volume/ area from BJH desorption method; volume= $V_{meso}+ V_{macro}$ and area= $S_{meso}+ S_{macro}$

Average pore hydraulic radius= V_{ultra}/ S_{ultra} from MP method

Average pore width= 4 V_{tot}/ SSA from BET

The average pore width was measured by ($\frac{4\,V_{tot}}{SSA}$), which decreases with increasing GNP concentration up to 50% which was (12.195 nm). But it increases (13.0345 nm) for 70% GNP sample, then it decreases again for 90% GNP sample which reaches (7.98 nm). As observed from table 4.6, the average pore width decreases with increasing SSA. This explains why 90% GNP sample had the smallest average pore width.

As expected from nitrogen isotherms, all samples contained mesopores which was proved by calculating the average pore width and the average BJH pore diameter. The dominant pore for 30% GNP, 50% GNP and 90% GNP was mesopores, which had 62%, 57.6% and 66%, respectively relative to the total pore volume for each sample. However, macropores were dominant for 10% GNP and 70% GNP, with values 52.37% and 51.09%, respectively.

The specific capacitance values increase with increasing GNP concentrations due to increase SSA and decrease pore size because the pore size of ultra- micropore are more compatible with ions sizes (OH^-, K^+) [18, 19, 49]. Therefore, CV results can be explained as following: at low scan rates all pores contributed in charge and discharge processes. So, the sample which had the highest SSA, meso, micro and ultra- micropores gave the highest values of C_S which was for the 90% GNP sample. However, at high scan rates, only meso and macro pores with high total pore volume and high accessible area had the highest contribution on charging process because not all ions have enough time to penetrate all pores. These reasons explain the decrease in C_S values for 90% GNP sample and why 70% GNP sample had the highest C_S values at 50 and 100 mV/s.

Also, by GCD method the sample of 90% weight concentration of GNPs has the highest values of C_S at different specific currents, because it contains high SSA and high micropores which match the size of the ions. So, the number of ions which penetrate into the pores increases, hence,

more time is needed to fill high number of the pores. This means that longer charge/ discharge processes which causes an increase in specific capacitance.

As observed in EIS method, at high frequency region, ESR values decrease with increasing GNP concentration up to 70% of GNP weight, then it increases for 90% GNP samples. This is due to the dependence of ESR value on pore volume, variety of pore types and PSD. ESR value decreases with increasing pore size, and decreases with increasing the number of accessible pores [17, 19, 80], this explains the smallest value of ESR for 70% GNP sample. However, 90% GNP sample has more micropores which will fill faster relative to the other types of pores, according to the following equation, $\tau = L^2/D$; where L is the ion transport length and D is the ion transport coefficient. For this reason, part of ions penetrates easier into the micropores while the rest ions face difficulties to penetrate the other types of pores due to collisions between them because of the randomly movement and part of the pores are accessible because they do not have enough time to fill all pores, this causes increasing the ESR value [17, 18]. On the other hand, at low frequency region, the resistance values increase for the samples because the ions can go deeper into all pores to fill meso and macropores into the electrode surface because they have enough time for penetration. Furthermore, the C_S value increases with decreasing frequency values which reaches its highest value at the lowest value of frequency because all pores contribute on charge/ discharge processes.

Chapter Five
Conclusion

We have successfully prepared symmetrical SC based on binder- free-electrodes with different contents of CNFs and GNPs. Firstly, we have studied the electrochemical characterization by using different methods: CV, GCD and EIS methods. Secondly, we have studied the structure, morphology and PSD for the prepared electrodes by using BET, BJH, Harkins- Jura and MP methods. The structural behavior is used to explain the electrochemical behavior of the CNF/ GNP composites.

The C_S value was found to increase with increasing GNP weight concentration, this is due to increase SSA, meso, micro and ultra-micropore areas and volumes. The highest value of C_S was for 90% GNP sample, which achieved 119.7 F/g at scan rate of 5 mV/s, 54.6 F/g at 0.43 A/g specific current and 123.1 F/g at 10 mHz by CV, GCD and EIS methods, respectively. This is due to its high SSA of 665.93 m^2/g and shorter diffuse length of ions because of its small pore size relative to the other samples.

Adding different amount of GNPs to CNFs also effect on the conductivity of the prepared electrodes. The weight concentration of GNP which gives the smallest ESR value of 0.632 Ω was 70%. This is explained according to its high total pore volume of 1.72 cm^3/g, high macropore volume, high number of pores and variety of PSD. So, more accessible pores are available for the ions to move freely into pores.

Ragone plot was constructed by calculating power and energy densities for CNF/ GNP composites at different specific currents. The highest power and energy densities were for 70% weight concentration of GNPs due to its small ESR value, small voltage drop value and high discharge time. The highest power density was 1095.4 W/kg at high current of 100 mA, while the highest energy density was 5.26 Wh/kg at current of 30 mA.

As expected CNF/ GNP composites had enhanced the properties of SC. The aim was to achieve small ESR to increase the power density and achieve high C_S to increase the energy density. The influence of adding GNPs was increasing SSA, total pore volume and increasing ultra-micropores. These reasons increased the C_S values of CNF/ GNP composites, hence, the energy density increased. Also, GNPs join CNFs together without blocking the pores like adding polymers. However, adding CNFs had the influence on decreasing ESR value of GNPs, hence, the power density increased.

For more performance, the best concentration of CNFs and GNPs can be used by different aqueous electrolytes or by using gel electrolyte to choose the best electrolyte which will give the best power and energy densities.

References

[1] V. Ganesh, S. Pitchumani and V. Lakshminarayann. (2006). ***New symmetric and asymmetric supercapacitors based on high surface area porous nickel and activated carbon***. **J. Power Sources** 158: 1523- 1532.

[2] Ch. Tao and D. Liming. (2013). ***Carbon nanomaterials for high-performance supercapacitors*. J. Materials Today** 16: 272- 280.

[3] A. Daraghmeh, Sh. Hussain, L. Servera, E. Xuriguera, A. ***Cornet and A. Cirera. (2017). Impact of binder concentration and pressure on performance of symmetric CNFs based supercapacitors***. **J. Electrochimica Act 245**: 531- 538.

[4] W. Chen, M. Beidaghi, V. Penmatsa, K. Bechtold, L. Kumari, K. Z. Li and Ch. Wang. (2010). ***Integration of Carbon Nanotubes to C- MEMS for On- chip Supercapacitors***. **J. Transactions on nanotechnology** 9: 734- 740.

[5] R. B. Marichi, V. Sahu, R. K. Sharma and G. Singh. (2017). **Efficient, Sustainable and Clean Energy Storage in Supercapacitors Using Biomass- Derived Cabon Materials.** B. Handbook of Ecomaterials 1. Springer- Nature: 1- 26.

[6] H. Yang. (2013). **Graphene- based Supercapacitors for Energy Storage Applications**. Master Thesis. Ohio State University. Athens. Ohio. United States.

[7] A. Daraghmeh. (2017). **Advances in carbon nanofiber- based supercapacitors.** Doctoral Thesis. Barcelona University. Barcelona. Catalonia. Spain.

[8] Mao. Lu. (2013). **Graphene- based materials for supercapacitor electrodes.** Doctoral Thesis. National University of Singapore. Singapore.

[9] D. P. Dubal, O. Ayyad, V. Ruiz and P. Gomez- Romero. (2015). ***Hybrid energy storage: the merging of battery and supercapacitor chemistries***. **J. Chem. Soc.** Rev 44: 1777- 1790.

[10] M. Salanne, B. Rotenberg, K. Naoi, K. Kaneko, P. L. Taberna, C. P. Grey and B. Dunn. (2016). **Efficient storage mechanisms for building better supercapacitors. J. Nature Energy 1**: 16070.

[11] Li. Xiaofei. (2012). **Composite Electrode for Electrochemical Supercapacitors.** Master Thesis. McMaster University. Hamilton. Ontario. Canada.

[12] A. Singh, A. J. Roberts, R. C. T. Slade and A. Chandra. (2014). ***High electrochemical performance in asymmetric composite and graphene nanoplates as electrodes***. **J. Materials Chemistry** A 2: 16723- 16730.

[13] W. Lu, K. Henry, C. Turchi and J. Pellegrino. (2008). ***Incorporating Ionic Liquid Electrolytes into Polymer Gels for Solid- State Ultracapacitors*. J. Electrochemical Society** 155: A361- A3675.

[14] M. Beidaghi, Zh. Wang, L. Gu and Ch. Wang. (2012). ***Electrostatic spray deposition of graphene nanoplatelets for high- power thin- film supercapacitor electrodes.*** **J. Solid State Electrochem** 16: 3341- 3348.

[15] G. Qiaohui, Zh. Xiaoping, Li. Xiaoyan, Ch. Shuiliang, S. Agarwal, G. Andreas and H. Haoqing. (2009). ***Supercapacitors based on hybrid carbon nanofibers containing multiwalled carbon nanotubes***. **J. Materials Chemistry** 19: 2810- 2816.

[16] M. D. Stoller and R. S. Ruoff. (2010). ***Best practice methods for determining an electrode material's performance for Ultracapacitors***. **J. Energy & Environmental Science** 3: 1294- 1301.

[17] R. Kotz and M. Carlen. (2000). ***Principles and applications of electrochemical capacitors.*** **J. Electrochimica Acta** 45: 2483- 2498.

[18] A. Daraghmeh, Sh. Hussain, I. Saadeddin, L. Servera, E. Xuriguera, A. Cornet and A. Cirera. (2017). ***A study of Carbon Nanofibers and Active Carbon as Symmetric Supercapacitor in Aqueous Electrolyte: A Comparative Study***. **J. Springer** 12: 639- 648.

[19] F. Beguin, V. Presser, A. Balducci and E. Frackowiak. (2014). ***Carbons and Electrolytes for Advanced Supercapacitors***. **J. Advanced Materials** 26: 2219- 2251.

[20] S. Biniak, A. Swiatkowski and M. Pakula. (2001). ***Electrochemical studies of phenomena at active carbon- electrolyte solution interface***. **J. Chemistry and Physics of Carbon** 27: 126- 216.

[21] S. Bose, T. Kuila, A. K. Mishra, R. Rajasekar, N. H. Kim and J. H. Lee. (2012). ***Carbon- based nanostructured materials and their composites as supercapacitor electrodes***. **J. Materials Chemistry** 22: 767- 784.

[22] V. Ruiz, C. Blanco, M. Granda, R. Menendez and R. Santamaria. (2007). ***Influence of Electrode Preparation on the Electrochemical Behavior of Carbon- Based Supercapacitors***. **J. Appl Electrochem** 37: 717721.

[23] Sh. Chao, Hu. Lintong, Gu. Kai, Li. Huiqiao and Zh. Tianyon. (2017). ***Highly Porous Carbon Nanoplateletes Microstructure Derived from Biomass Waste for High- Performance Supercapacitors in Universal Electrolyte.*** **J. Advanced Science News** 1: 1600011.

[24] M. Toupin, Th. Brousse and D. Belanger. (2004). ***Charge Storage Mechanism of MnO_2 Electrode Used in Aqueous Electrochemical Capacitor***. **J. Chem. Mater** 16: 3184- 3190.

[25] A. Daraghmeh, Sh. Hussain, L. Servera, E. Xuriguera, M. Blanes, F. Ramos, A. Cornet and A. Cirer. (2017). ***Flexible supercapacitors based on low- cost tape casting of high dense carbon nanofibers***. **J. Materials Research Express** 4: 025007.

[26] M. Mastragostinom, C. Arbizzani and F. Soavi. (2002). ***Conducting polymers as electrode materials in supercapacitors.*** **J. Solid State Ionics** 148: 493- 498.

[27] Q. Gao. (2013). **Optimizing carbon/ carbon supercapacitors in aqueous and organic electrolytes**. Thesis. University of Orle'ans. Orle'ans. France.

[28] X. Zhang, H. Zhang, Ch. Li, K. Wang, X. Sun and Y. Ma. (2014). ***Recent advances in porous graphene materials for supercapacitor applications*****. J. RSC Advances** 4: 45862- 45884.

[29] W. Raza, F. Ali, N. Raza, Y. Luo, Ki. H. kim, J. Yang, S. Kumar, A. Mehmood and E. E. Kwon. (2018). ***Recent advancements in supercapacitor technology*****. J. Nano Energy** 52: 441- 473.

[30] F. Belhachachemi, S. Raed and B. Davat. (2000). **A physical based model of power electric double- layer supercapacitors**. Conference record of 2000 IEEE (Institute of Electrical and Electronics Engineers). Rome. Italy: 3069- 3076.

[31] K. Jost, G. Dion and Y. Gogotsi. (2014). ***Textile energy storage in perspective***. **J. Material Chemistry A2**: 10776- 10787.

[32] V. Augustyn, P. Simon and B. Dunn. (2014). ***Pseudocapacitive oxide materials for high- rate electrochemical energy storage***. **J. Energy & Environmental Science 7**: 1597- 1614.

[33] M. Sh. Hong, S. H. Lee and S. W. Kim. (2002). ***Use of KCL Aqueous Electrolyte for 2 V Manganese oxide/ Activated Carbon Hybrid Capacitor***. **J. The Electrochemical Society** 5: A227- A230.

[34] A. Nishino. (1996). ***Capacitors: operating principles, current market and technical tends***. **J. Power Source** 60: 137- 147.

[35] H. E. Becker. (1957). **US. Patent 2 800 616**. General Electric.

[36] D. I. Boos. (1970). **US. Patent 3 536 963**. Standard Oil, SOHIO.

[37] M. Nakamura, M. Nakanishi and K. Yamamoto. (1996). ***Influence of physical properties of activated carbons on characteristics of electric double- layer capacitor*. J. Power Sources** 60: 225- 23.

[38] L. Demarconnay, E. Raymundo- Pinero and F. Benguin. (2010). ***Asymmetric carbon/ carbon supercapacitor operating at 1.6 V by using a neutral aqueous solution***. **J. Electrochem Communications** 12: 1275- 1278.

[39] X. Sun, X. Zhang and H. Zhang. (2012). ***A comparative study of activated carbon- based symmetric supercapacitors in Li_2SO_4 and KOH aqueous electrolytes.*** **J. Solid State Electrochem** 16: 2597- 2603.

[40] N. Yazdani and E. Brown. (2016). 3. **Carbon nanofibers in cement composites: Mechinical reinforcement**. **B**. Innovative Developments of Advanced Multifunctional Nanocomposities in Civil and Structural Engineering. Elsevier: 47- 58.

[41] A. Oberlin, M. Endo and T. Koyama. (1976). ***Filamentous growth of carbon through benzene decomposition.*** **J. Crystal Growth** 32: 335- 349.

[42] M. K. Seo, S. J. Park. (2009). ***Electrochemical characteristics of activated carbon nanofiber electrodes for supercapacitors***. **J. Materials Science and Engineering B164**: 106- 111.

[43] Yu. Wang, S. Serrano, J. J and S. Aviles. (2003). ***Raman characterization of carbon nanofibers prepared using electrospinning***. **J. Synthetic Metals** 138: 423- 427.

[44] J. Sun. Im, S. J. Kim, Ph. H. Kang and Y. S. Lee. (2009). ***The improved electrical conductivity of carbon nanofibers by fluorinated MWCNTs***. **J. Industrial and Engineering Chemistry** 15: 699- 702.

[45] M. Raimondo, L. Guadagno, L. Vertuccio, C. Naddeo, G. Barra, G. Spinelli, P. Lamberti, V. Tucci and Kh. Lafdi. (2018). ***Electrical conductivity of carbon nanofiber reinforced resins: Potentiality of Tunneling Atomic Force Microscopy (TUNA) technique***. **J. Composites Part B 143**: 148- 160.

[46] A. Askounis, Y. Yamada, T. Ikuta, K. Takahashi, Y. Takata and Kh. Sefiane. (2016). ***On the linear dependence of a carbon nanofiber thermal conductivity on wall thickness***. **J. AIP Advances** 6: 115119.

[47] F. Hoshi, K. Tsugawa, A. Goto, T. Ishikura, S. Yamashita, M. Yumura, T. Hirao, K. Oura and Y. Koga. (2001). ***Field emission and structure of aligned carbon nanofibers deposited by ECR- CVD plasma method.*** **J. Diamond and Related Materials 10**: 254- 259.

[48] B. Kumar, M. Asadi, D. Pisasale, S. S. Ray, B. A. Rosen, R. Haasch, J. Abiade, A. L. Yarin and A. S. Khojin. (2013). ***Renewable and metal-free carbon nanofiber catalysts for carbon dioxide reduction***. **J. Nature Communications 4**: 2819.

[49] P. Cataldi, A. Athanassiou and I. S. Bayer. (2018). ***Graphene Nanoplatelets- Based Advanced Materials and Recent Progress in Sustainable Applications***. **J. Applied Science 8**: 1438.

[50] M. K. Singh, M. Suleman, Y. Kumar and S. A. Hashmi. (2014). ***A novel configuration of electrical double layer capacitor with plastic crystal based gel polymer electrolyte and graphene nano- platelets as electrodes: A high rate performance.*** **J. Energy 80**: 1- 9.

[51] JS. Bonso, A. Rahy, SD. Perera, N. Nour, O. Seitz and YJ. Chabal. (2012). ***Exfoliated graphite nanoplateletes- V_2O_5 nanotube composite electrodes for supercapacitors***. **J. Power Sources 203**: 227- 32.

[52] Wu. Haung, T. Lawrence and Drzal. (2012). ***Graphene nanoplatelet paper as light- weight composite with excellent electrical and thermal conductivity and good gas barrier properties***. **J. Carbon 50**: 1135- 1145.

[53] A. Scida, S. Haque, E. Treossi, A. Robinson, S. Smerzi, S. Ravesi, S. Borin and V. Palermo. (2018). ***Application of graphene- based flexible antennas in consumer electronic devices***. **J. Materials Today 21**: 223- 230.

[54] S. Biswas, H. Fukushima and L.T. Drzal. (2011). ***Mechanical and electrical property enhancement in exfoliated graphene nanoplatelet/ liquid crystalline polymer nanocomposites***. **J. Composites Part A: Applied Science and Manufacturing 42**: 371- 375.

[55] S. Y. Kim, Y. J. Noh and J. Yu. (2015). ***Thermal conductivity of graphene nanoplatelets filled composites fabricated by solvent- free processing for the excellent filler dispersion and a theortical approach for the composites containing the geometrized fillers***. **J. Composites Part A: Applied Science and Manufacturing 69**: 219- 225.

[56] Sh. Ding, P. Si, X. W. Lou and D. H. Kim. (2011). ***An electrochemically formed three- dimensional structure of polypyrrole/ graphene nanoplatelets for high performance supercapacitors***. **J. Royal Society of Chemistry 1**: 1271- 1278.

[57] J. Zhu, S. Jasper and X. Zhang. (2017). 8. **Chemical characterization of electrospun nanofibers.** B. Electrospun Nanofibers. Woodhead publishing series: 181- 206.

[58] S. Lavrenzi and M. G. Santonicola. (2017). 7. **Impact response of advanced composite structures reinforced by carbon nanoparticles**. B. Dynamic Response and Failure of Composite Materials and Structures. Elsevier: 217- 235.

[59] Y. A. kim, T. Hayashi, M. Endo and M. S. Dresselhaus. (2013). **Carbon Nanofibers**. B. Handbook nano- materials. Springer: 233- 262.

[60] J. Wang, Zh. Zhang, Q. Zhang, J. Liu and J. Ma. (2018). ***Preparation and adsorption application of carbon nanofibers with large specific surface area,*** **J. Materials Science 53**: 16466- 16475.

[61] J. S. Bonso, G. D. Kalaw and J. P. Ferraris. (2014*).* ***High surface area carbon nanofibers derived from electrospun PIM-1 for energy storage applications***. **J. Materials Chemistry A 2**: 418- 424.

[62] R. N. Roa and S. S. Albaseer. (2018). 7. **Nanomaterials in Chromatographic Sample Preparations.** B. Nanomaterials in Chromatography. Elsevier: 201- 231.

[63] J. K. Fink. (2018). **Reactive Extrusion**. B. Reactive Polymers: Fundamentals and Applications 3. Elsevier: 449- 496.

[64] S. Dul, L. Fambri, C. Merlini, G. M. O. Barra, M. Bersani, L. Vanzetti and A. Pegoretti. (2017). ***Effect of graphene nanoplatelets structure on the properties of acrylonitrile- butadiene- styrene composites***. **J. Polymer Composites 40**: E285- E300.

[65] B. E. Conway, V. Birss and J. Wojtowicz. (1997). ***The role and utilization of pseudocapacitance foe energy storage by supercapacitors***. **J. Power Sources 66**: 1- 14.

[66] R. Farma, M. Deraman, Awitrus, I. A. Talib, R. Omar, J. G. Manjunatha, M. M. Ishak, N. H. Basri and B. N. M. Dolah. (2013). ***Physical and Electrochemical properties of Supercapacitor Electrodes Derived from Carbon Nanotube and Biomass***. **J. Electrochemical Science 8**: 257- 273.

[67] V. Khomenko, E. Frackowiak and F. Beguin. (2005). ***Determination of the specific capacitance of conducting polymer/ nanotubes composite electrodes using different cell configuration*****. J. Electrochimica Acta 50**: 2499- 2506.

[68] Ch. Hu. (2008). **Fluid Coke Derived Activated Carbon as Electrode Material for Electrochemical Double Layer Capacitor**. Master Thesis. University of Toronto. Toronto. Ontario. Canada.

[69] Jaidev, R. I. Jafri, A. K. Mishra and S. Ramaprabhu. (2011). ***Polyaniline- MnO_2 nanotubes hybrid nanocomposite as supercapacitor electrode material in acidic electrolyte***. **J. Electronic Supplementary Material 21**: 17601- 17605.

[70] M. E. Orazem and B. Tribollet. (2017). 5. **Electrochemistry**. B. Electrochemical Impedance Spectroscopy 2. WILEY. 1- 768.

[71] D. V. Riberio and J. C. C. Abrante. (2016). ***Application of electrochemical impedance spectroscopy (EIS) to monitor the corrosion of reinforced concrete: A new approach.*** **J. Construction and Building Materials 111**: 98- 104.

[72] L. D. Gelb and K. E. Gubbins. (1998). ***Characterization of Porous Glasses: Simulation Models, Adsorption Isotherms, and the Brunauer- Emmett- Teller Analysis Method.*** **J. Langmuir 14**: 2097- 2111.

[73] A. S. Levy and D. Avnir. (1993). ***The Brunauer- Emmett- Teller Equation and the Effect of Lateral Interactions: A Simulation Study***. **J. Langmuir 9**: 2523- 2529.

[74] S. Brunauer, P. H. Emmett and E. Teller. (1938). ***Adsorption of Gases in Multimolecular layers*****. J. American Chemical Society 60**: 309- 319.

[75] M. H. Marzbali and M. esmaieli. (2017). ***Fixed bed adsorption of tetracycline on a mesoporous activated carbon: Experimental study and neuro- fuzzy modeling.*** **J. Applied Research and Technology (JART) 15**: 454- 463.

[76] A. Galarneau, D. Mehlhorn, F. Guenneau, B. Coasne, F. Villemot, D. Minoux, C. Aquino and J. P. Dath. (2018). ***Specific Surface Area Determination for Microporous/ Mesoporous Materials: The case of Mesoporous FAU- Y Zeolites*****. J. HAL 34**: 14134- 14142.

[77] T. Horikawa, D. D. Do and D. Nicholson. (2011). ***Capillary condensation of adsorbates in porous materials***. **J. Advances in Collide and Interface Science 164**: 40- 58.

[78] P. Klobes, K. Meyer and R. G. Munro. (2006). **B. Porosity and Specific Surface Area Measurements for Solid Materials**. NIST publication 960: 1- 89.

[79] Y. Zheng. (2008). **Evaluation of a New Method to Estimate the Micropore Volume and External Area of Single- walled Carbon Nanotubes**. Master Thesis. University of Tennessee. Knoxville. Tennessee. United State.

[80] Ch. Sh. Lim, K. H. Teoh, Ch. W. Liew and S. Ramesh. (2014). ***Electric double layer capacitor based on activated carbon electrodeand biodegradable composite polymer electrolyte***. **J. Ionics 20**: 251- 258.

[81] J. W. Graydon, M. Panjehshahi and D. W. Kirk. (2014). ***Charge redistribution and ionic mobility in the micropores of supercapacitors***. **J. Power Sources 245**: 822- 829.

[82] R. A. P. Jayawickramage and J. P. Ferraris. (2019). ***High performance supercapacitors using lignin based electrospun carbon nanofiber electrodes in ionic liquid electrolytes***. **J. Nanotechnology 30**: 155402.

[83] S. K. Meher, P. Justin and G. R. Rao. (2011). ***Microwave- Mediated Synthesis for Improved Morphology and Pseudocapacitance Performance of Nickel Oxide.*** **J. ACS Appl. Mater. Interfaces 3**: 2063- 2073.

[84] M. Jayalakshmi and K. Balasubramanian. (2008). ***Simple Capacitors to Supercapacitors- An Overview.*** **J. Electrochemical Science 3**: 1196- 1217.

[85] W. Hao, W. Xianyou, j. Lanlan, Wu. Chun, Zh. Qinglan, Li. Xue, Hu. Ben'an and Yi. Lanhua. (2013). ***The effects of electrolyte on supercapacitive performance of activated calcium carbide- derived carbon***. **J. Power Sources 226**: 202- 209.

[86] I. Yang, S. G. Kim, S. H. Kwon, M. S. Kim and Ji. Ch. Jung. (2017). ***Relationships between pore size and charge transfer resistance of carbon aerogels for organic electric double- layer capacitor electrodes***. **J. Electrochimica Acta 223**: 21- 30.

[87] K. Morishige and N. Tateishi. (2003). ***Adsorption hysteresis in ink-bottle pore.*** **J. Chem. Phys. 119**: 2301.

[88] G. Leofanti, M. Padovan, G. Tozzola and B. Venturelli. (1998). ***Surface area and pore texture of catalysts***. **J. Catalysis Today 41**: 207- 219.

جامعة النجاح الوطنية

كلية الدراسات العليا

إستخدام مخلوط ألياف الكربون النانوية: صفائح الجرافين النانو كأقطاب للمكثف المثالي بإستخدام هيدروكسيد البوتاسيوم

إعداد

صابرين صبري جرار

إشراف

د. علان دراغمة

د. إياد سعد الدين

قدّمت هذه الأطروحة إستكمالاً لمتطلبات الحصول على درجة الماجستير في الفيزياء، بكلية الدراسات العليا، في جامعة النجاح الوطنية، نابلس– فلسطين.

2020

إستخدام مخلوط ألياف الكربون النانوية: صفائح الجرافين النانو كأقطاب للمكثف المثالي بإستخدام هيدروكسيد البوتاسيوم

إعداد

صابرين صبري جرار

إشراف

د. علان دراغمة

د. إياد سعد الدين

الملخص

في هذه الأطروحة، المواسع المثالي الذي يتكون من أقطاب مركبة متوازية تم تحضيره باستخدام تراكيز مختلفة من ألياف النانو كربون وصفائح النانو جرافين. هذه النسب من ألياف النانو كربون: صفائح النانو جرافين تم تغييرها من 90٪ : 10٪ الى 10٪ : 90٪، بالترتيب من خلال زيادة 20٪ في كل مرة.

الخصائص الالكتروكيميائية تم تفسيرها من خلال قياس الجهد الدوري، طريقة الشحن والتفريغ وطريقة قياس المقاومة الاكتروكيميائية باستخدام المحلول المائي (1 مول) هيدروكسيد البوتاسيوم.

قيم كثافة السعة كانت تتزايد مع زيادة تركيز صفائح النانو جرافينز بحيث زادت من 47,0 الى 119,7 فاراد/غرام عندما زادت كمية صفائح النانو جرافين من 10٪ الى 90٪ عند معدل التنقل 5 ملي فولت/ثانية باستخدام طريقة قياس الجهد الدوري.

كثافة القدرة وكثافة الطاقة تم حسابها من خلال طريقة الشحن والتفريغ. قيم كثافة القدرة وكثافة الطاقة ازدادت مع زيادة تركيز صفائح النانو جرافين حتى وصلت النسبة الى 70٪، ثم قلت عند زيادة تركيز صفائح النانو جرافين الى 90٪. كثافة القدرة زادت من 528,33 الى 1095,96 واط /كغم، ثم قلت الى 956،97 واط /كغم. كثافة الطاقة زادت من 2,32 الى 5,26 واط ساعة /كغم، ثم قلت الى 5,.5 واط ساعة/ كغم.

أخيرا"، المقاومة المكافئة تم حسابها باستخدام طريقة قياس المقاومة الالكتروكيميائية، بحيث أن قيم المقاومة المكافئة قلت مع زيادة تركيز صفائح النانو جرافين حتى أصبحت النسبة 70٪، ثم ازدادت عندما زادت نسبة صفائح النانو جرافين الى 90٪. المقاومة المكافئة قلت من 1,48 الى 0.632 Ω ثم ازدادت الى 1,.26 Ω عندما أصبحت نسبة صفائح النانو جرافين 90٪.

المركب تم تحسينه من ناحية كثافة السعة، كثافة القدرة، كثافة الطاقة والمقاومة المكافئة كانت للمركب المكون من 30٪ : 70٪ من الياف النانو كربون: صفائح النانو جرافين. حيث أن هذا المركب يمتلك 102,2 فاراد/غرام، 1095,43 واط /كغم، 5,26 واط ساعة/ كغم و0,632 Ω، بالترتيب.

كثافة مساحة السطح، توزيع حجم المسامات وخصائص السطح للمركبات المحضرة تم شرح خصائصها باستخدام الطرق التالية: برونر– ايميت– تيلر، بارت– جونر– هالندا، هاركنز– جورا ومجهر المسح الالكتروني.

قيم كثافة مساحة السطح ازدادت مع زيادة تركيز صفائح النانو جرافين. بحيث أنها زادت من 271,27 الى 665,93 م^{٢}/غرام عندما تغيرت نسبة صفائح النانو جرافين من 10٪ الى 90٪.

الحجم الكلي للمسامات زاد مع زيادة تركيز صفائح النانو جرافين حتى أصبحت 70٪، ثم قل عندما أصبحت النسبة 90٪. الحجم الكلي للمسامات زاد من 1,22 الى 1,72 سم^{٣}/غرام، ثم قل الى 1,33 سم^{٣}/غرام.

المسامات التي حجمها مايكرو(مجهرية)، فائقة المجهرية والمتوسطة الحجم زادت مع زيادة نسبة صفائح النانو جرافين من 10٪ الى 90٪. المسامات المجهرية زادت من 0,023 الى 0,28 سم^{٣}/غرام، وفائقة المجهرية زادت من 0,023 الى 0,08 سم^{٣}/غرام والمسامات المتوسطة الحجم زاد حجمها من 0,55 الى 0,88 سم^{٣}/غرام.

أخيراً، حجم المسامات الكبيرة (الماكرو) قلت مع زيادة نسبة صفائح النانو جرافين من 10٪ الى 30٪ بحيث قلت من 0,64 الى 0,29 سم^{3}/غرام. ثم ازدادت الى أن أصبح تركيز صفائح النانو جرافين 70٪ بحيث زاد الحجم الى 0,88 سم^{3}/غرام، ثم قل الحجم مجدداً عندما أصبح تركيز صفائح النانو جرافين 90٪ (0,33 سم^{3}/غرام).

أفضل المركبات التي تم تحضيرها التي تمتلك أفضل خصائص للسطح عندما كانت نسبة صفائح النانو جرافين 70٪ بحيث أنها تمتلك أعلى حجم كلي للمسامات، أعلى حجم للمسامات الكبيرة (الماكرو)، وأيضاً تمتلك كثافة مساحة السطح، حجم المسامات المجهرية (الميكرو)، حجم المسامات فائقة المجهرية وحجم المسامات المتوسطة عالية نسبياً. حيث أن هذا المركب يمتلك 1,72 سم^{3}/غرام، 0,88 سم^{3}/غرام، 528,52 م^{2}/غرام، 0,0614 سم^{3}/غرام و0,78 سم^{3}/غرام، بالترتيب.